ERNEST ORLANDO LAWRENCE
BERKELEY NATIONAL LABORATORY

Natural Gas Variability In California: Environmental Impacts And Device Performance

Combustion Modeling of Pollutant Emissions From a Residential Cooking Range

S.R. Tonse
TST Scientific Consulting, Orinda CA

B.C. Singer
Environmental Energy Technologies Division
Indoor Environment Department

July 2011

Direct funding of this research was provided by the California Energy Commission through Contract 500-05-026. Additionally, this work was supported by the Director, Office of Science, Office of Basic Energy Sciences, of the U.S. Department of Energy under Contract No. DE-AC02-05CH11231.

Disclaimer[1]

This document was prepared as an account of work sponsored by the United States Government. While this document is believed to contain correct information, neither the United States Government nor any agency thereof, nor The Regents of the University of California, nor any of their employees, makes any warranty, express or implied, or assumes any legal responsibility for the accuracy, completeness, or usefulness of any information, apparatus, product, or process disclosed, or represents that its use would not infringe privately owned rights. Reference herein to any specific commercial product, process, or service by its trade name, trademark, manufacturer, or otherwise, does not necessarily constitute or imply its endorsement, recommendation, or favoring by the United States Government or any agency thereof, or The Regents of the University of California. The views and opinions of authors expressed herein do not necessarily state or reflect those of the United States Government or any agency thereof or The Regents of the University of California.

Ernest Orlando Lawrence Berkeley National Laboratory is an equal opportunity employer.

Legal Notice

This report was prepared as a result of work sponsored by the California Energy Commission (Commission). It does not necessarily represent the views of the Commission, its employees, or the State of California. The Commission, the State of California, its employees, contractors, and subcontractors make no warranty, express or implied, and assume no legal liability for the information in this report; nor does any party represent that the use of this information will not infringe upon privately owned rights. This report has not been approved or disapproved by the Commission nor has the Commission passed upon the accuracy or adequacy of the information in this report.

Notice about Report and Appendix Availability

This report has been submitted to the California Energy Commission (CEC). It is anticipated that a version of the report – containing the same technical information but potentially differing in presentation based on changes made by CEC technical editors – will be published by the Energy Commission. If published by CEC, the report should be available at the following site: http://www.energy.ca.gov/reports/.

---

[1] Disclaimer included verbatim as required by LBNL RPM Section 5.02.03. United State Government sponsorship refers to the management contract noted in the Acknowledgments. The specific work described in this report was funded by the California Energy Commission through contract 500-05-026.

Acknowledgments

The authors acknowledge with appreciation the following contributions: Professor Hai Wang (University of Southern California) for graciously providing the chemical mechanism, and Dr. Nancy J. Brown (Lawrence Berkeley National Laboratory) for the use of the Mariah parallel computing cluster.

The authors thank all members of the Project Advisory Committee who contributed their time, knowledge, and many specific suggestions that improved this work. We greatly appreciate the technical editorial contributions of Mark Wilson.

Direct funding of this research was provided by the California Energy Commission through Contract 500-05-026. Additionally, this work was supported by the Director, Office of Science, Office of Basic Energy Sciences, of the U.S. Department of Energy under Contract No. DE-AC02-05CH11231.

Table of Contents

List of Figures

List of Tables

Abstract

As part of a larger study of liquefied natural gas impacts on device performance and pollutant emissions for existing equipment in California, this report describes a computer modeling study of a partially premixed flame issuing from a single cooktop burner port. The model consisted of a reactive computational fluid dynamics three-dimensional spatial grid and a 71-species chemical mechanism with propane combustion capability. Simulations were conducted with a simplified fuel mixture containing methane, ethane, and propane in proportions that yield properties similar to fuels distributed throughout much of California now and in recent years (baseline fuel), as well as with two variations of simulated liquefied natural gas blends. A variety of simulations were conducted with baseline fuel to explore the effect of several key parameters on pollutant formation and other flame characteristics. Simulations started with fuel and air issuing through the burner port, igniting, and continuing until the flame was steady with time. Conditions at this point were analyzed to understand fuel, secondary air and reaction product flows, regions of pollutant formation, and exhaust concentrations of carbon monoxide, nitric oxide and formaldehyde.

A sensitivity study was conducted, varying the inflow parameters of this baseline gas about real-world operating conditions. Flame properties responded as expected from reactive flow theory. In the simulation, carbon monoxide levels were influenced more by the mixture's inflow velocity than by the gas-to-air ratio in the mixture issuing from the inflow port.

Additional simulations were executed at two inflow conditions—high heat release and medium heat release—to examine the impact of replacing the baseline gas with two mixtures representative of liquefied natural gas. Flame properties and pollutant generation rates were very similar among the three fuel mixtures.

Keywords: Carbon monoxide, indoor air quality, liquefied natural gas, nitrogen oxide, combustion modeling

Executive Summary

Introduction

Concerns over carbon dioxide emissions are driving up demand for fuels in which a smaller fraction of the produced energy is a result of carbon combustion. As a result, demand for natural gas is expected to grow, since approximately half of its produced energy is a result of hydrogen oxidation, which produces water instead of carbon dioxide. The U.S. Department of Energy expects that 9 out of 10 new power plants in the nation will use natural gas. Natural gas consumption in the United States is currently 23 trillion cubic feet/year, 3 trillion of which is imported. Of this, about 0.5 trillion is supplied by tankers in the form of liquefied natural gas (LNG), the remainder being mainly pipeline imports from Canada. Liquefied natural gas imports are expected to grow, and consumption in California and other coastal states likely will be higher than the national average.

Natural gas comes in a wide variety of compositions and heating values (the amount of heat produced from a fixed amount of gas.). Imported LNG typically contains more energy per unit volume than the natural gas that in the past has been distributed in California. Anticipating increasing use of liquefied natural gas in California, the California Energy Commission requested research to assess the potential impacts of this change.

Lawrence Berkeley National Laboratory and the Gas Technology Institute are working in collaboration to assess these impacts. Lawrence Berkeley National Laboratory is focusing on residential appliances and air quality, while the Gas Technology Institute focuses on industrial burners. This report presents the results of a computer-modeling study of residential cooking range flames conducted as part of the research study. The intent of this work was to construct and analyze a computer-based model of a range-top burner flame to supplement data acquired through experimental observation of pollutant emissions.

Task Method

This modeling study's scientific goal is to increase understanding of the impacts of natural gas energy supply rate and composition on device performance and pollutant emissions. For this modeling study, gas composition was set as a mixture of methane, ethane, and propane. These mixtures are simplified, but the compositions reflect the overall physical properties representative of either current supplies from domestic sources ("baseline" natural gas) or liquefied natural gas blends.

The modeling tool used for this study is a reactive computational fluid dynamics computer program that represents the physical domain of the flame with a three-dimensional spatial grid. Due to computational constraints, only a single flame (issuing from a single port) was modeled, rather than the entire ring of flames from a real-world burner. By symmetry the expectation is that the multiple flames should be very similar, although it is acknowledged that any inter-flame interaction will not be captured. The modeling grid covers the physical extent of a single flame and its surroundings. Similar to real-world residential burners, in which a portion of the air for combustion is mixed within the burner head prior to issue from the port (primary air),

the simulation includes a partially premixed gas-air mixture entering the main grid through a horizontal inflow port, resulting in a fuel-rich premixed flame. The remaining air necessary to complete combustion is obtained from the open atmosphere (secondary air), and results in a diffusion flame or non-premixed flame, just downstream of the premixed flame. These regions can be distinguished when observing a range-top residential burner in one's own kitchen. Before commencing the computer simulation, each grid cell is assigned an initial temperature, pressure, velocity, and mixture of individual gaseous chemical species.

Starting from an initial time, the state of the system is advanced in discrete time steps. At every time step the physical and chemical processes that occur within real flames are simulated by numerical equations. The simulation is considered complete when the flame attains a steady appearance. This fully developed simulated flame provides data on general properties of the flame and gas flows, and spatial distribution and production of carbon monoxide, nitric oxide, and formaldehyde.

A series of such computer simulations were conducted, varying the gas composition of the fuel and the heat-release rate of the burner between simulations. The heat-release rate was manipulated by changing the velocity though the inflow port and also by changing the relative ratios of fuel and primary air.

Task Objectives

The specific objective and focus areas were as follows:

1. Conduct simulations with a baseline gas composition to understand:
    a) The internal features of the flame, including mapping of exhaust gas flow velocity and direction, mixing of secondary air with partial combustion products of fuel and primary air.
    b) Formation, location, and overall emissions of carbon monoxide, nitric oxide, and formaldehyde.
2. Using baseline gas, conduct a sensitivity study in which the inflowing gas parameters were varied about real-world operating conditions. During this study the port velocity and fuel air mixture were varied independently. The objective was to determine the degree to which flame properties and other outputs vary as the inputs are changed.
3. Select two additional gases similar in composition to those used in the experimental sub-tasks of this study. The criteria for specifying these fuels were to introduce significant variation in the relative amounts of ethane and propane and also in heating value. Compare simulation results in which gases are interchanged while other parameters were held constant.

Task Outcomes

The flame resulting from a typical simulation had the smooth, laminar appearance characteristic observed in range-top burner flames. A portion of the combustion was premixed, using air mixed with the gas issuing from the inlet port. The remainder of combustion was completed with outside atmospheric air. The hottest region of the flame was seen to be just above the inlet

port. This also was the region with the highest carbon monoxide concentrations and the highest thermal nitric oxide production.

During the sensitivity study (seven simulations with baseline gas), the inflow rate and fuel-to-air ratio were varied. Among the trends seen: increasing inflow velocity resulted in longer flame length, longer distance from the port to the point where burning commenced, and farther flame extent in the horizontal direction. Increasing fuel-to-air ratio (keeping velocity constant) resulted in a larger flame, with the flame front farther from the port. The unburned region between the inlet port and flame was angled more sharply upward, possibly because of the increased combustion rate. A single simulation conducted with a doubled heat delivery rate showed the horizontal extent of the flame larger, as expected, but flame height did not change as significantly.

In all of the simulations, the region of highest carbon monoxide concentration was in the afore-mentioned region of high temperature just above the inlet port. Keeping fuel-to-air ratio constant and increasing inlet port velocity, carbon monoxide was seen to come increasingly from this region.

Velocity had a stronger influence on the spatial distribution of carbon monoxide than did the fuel-to-air ratio.

Nitric oxide increased with both increasing inlet velocity and increasing fuel-to-air ratio. The spatial distribution of nitric oxide showed regions of high concentration near the inlet, particularly above the flame.

In the model, formaldehyde was largely consumed within the flame and only insignificant quantities (parts-per-billion levels) exited the top of the simulation grid. Laboratory studies of formaldehyde production in Bunsen flames (at parts per million levels) conclude that formaldehyde as a pollutant results mainly from cooling of the flame by quenching near surfaces that conduct heat away, thereby suppressing reactions responsible for removing formaldehyde. To accurately reproduce this in the model would require refinements and additional simulations beyond the scope of the work.

Six simulations (three at medium and three at high heat release) were conducted to compare baseline fuel to two simulated LNG blends. The two LNGs had heating values and Wobbe numbers (a measure of energy content delivered through a fixed orifice) higher than the baseline fuel. From spatial plots of temperature, carbon monoxide, and nitric oxide, some difference in spatial patterns was seen between the cases but nothing indicated that the basic flame properties were significantly different. When carbon monoxide and nitric oxide pollutant concentrations at the top of the simulation space were integrated and summed, it was seen that the simulated LNG fuels had slightly higher pollutant emissions.

Conclusions

The computer model reproduces the general characteristics of the flame. A sensitivity study indicated that flame properties and pollutant levels changed gradually as the heat release in the model is varied, and follows trends that are intuitively expected. No sudden changes or

transitions in flame behavior were observed in the sensitivity study. For the flame conditions studied, a high-temperature region located above the port was responsible for an increasing fraction of overall carbon monoxide production as inflow velocity was increased. The same region is also responsible for most of the thermal nitrogen oxide production. Further study of this area with both a modeling component and an experimental component may be instructive. Formaldehyde is almost completely consumed within the flame, and concentrations leaving the simulation grid are negligible.

Differences in flame properties and pollutant levels seen when interchanging LNGs with the baseline gas appear to be primarily as a result of the higher heating value of the LNGs, and not directly as a result of the differing proportions of methane, ethane, and propane. An investigation of production, destruction, and interaction between intermediate species along the oxidation paths of methane, ethane, and propane qualitatively explains why the carbon monoxide production is so similar for all three fuel mixtures.

Benefits to California

This research is helping to lay the groundwork for maintaining a safe and reliable natural gas supply in California. The proactive investigation of potential impacts of new supplies, including LNG, will allow California to better understand the impacts of fuel quality on operability and pollutant emission levels for the existing population of appliances in the state. The results presented in this report will be used to assess potential impacts on indoor exposures associated with gas cooking burners and outdoor air quality, including ozone and secondary organic aerosol.

1.0 Background

Concerns over carbon dioxide (CO_2) emissions are driving up demand for fuels in which a smaller fraction of the produced energy is a result of carbon combustion. As a result, demand for natural gas is expected to grow, since approximately half of its produced energy is a result of hydrogen oxidation, which produces water instead of carbon dioxide. The U.S. Department of Energy expects that 9 out of 10 new power plants in the nation will use natural gas. Natural gas consumption in the United States is currently 23 trillion cubic feet/year, 3 trillion of which is imported. Of this, about 0.5 trillion cubic feet/year is supplied by tankers in the form of liquefied natural gas (LNG), the remainder being mainly pipeline imports from Canada. Liquefied natural gas imports are expected to grow, and consumption in California and other coastal states likely will be higher than the national average.

Natural gas comes in a wide variety of compositions and heating values (the amount of heat produced from a fixed amount of gas). Imported LNG typically contains more energy per unit volume than the natural gas that in the past has been distributed in California.

The California Energy Commission's Public Interest Natural Gas Research program has the charge to address significant natural gas issues in the State of California. One of the most important issues is the anticipated growth of new gas supplies—principally including LNG from Pacific Rim exporters—required to meet growing demand across the Western United States. As mentioned earlier, these new fuels can differ in composition and have higher heating values and Wobbe numbers (a measure of energy content delivered through a fixed orifice) compared with recent historical supplies. These differences raise questions about the potential impacts of using LNG with the existing population of end-use equipment. Impacts of concern include safety, performance, service life, and air pollutant emissions.

Lawrence Berkeley National Laboratory (LBNL) and the Gas Technology Institute (GTI) are conducting research to support a broad examination of the potential air quality and end-use device performance impacts of LNG use in California. Lawrence Berkeley National Laboratory and GTI jointly developed a research plan that included experimental burner evaluations, statistical analysis and modeling of results, combustion modeling, outdoor air quality modeling, and indoor exposure modeling assessments. The Gas Technology Institute focused on the experimental evaluation of industrial and commercial burners. Lawrence Berkeley National Laboratory focused on residential appliance burners and air quality impacts.

This document reports on computer modeling work conducted as part of Task 10 of the research study. The intent of this sub-task was to supplement data acquired through experimental observation of pollutant emission through the use of three-dimensional computer modeling of natural gas flames to gain insight on the flame properties and formation of pollutants. The primary technical work on this task was conducted by Dr. Shaheen Tonse, working as a sub-contractor to LBNL. Dr. Tonse consulted regularly with the LBNL principal investigator, Dr. Brett Singer, who provided guidance and coordination with other project elements.

1.1. Study Overview

This was a computer-based combustion modeling study to simulate natural gas flames in an idealized residential range-top burner appliance. These have simple Bunsen-like laminar flames, simple exterior geometry, and are used in most homes. Through a series of computer simulations in which conditions such as the gas composition of the fuel and heat-release rate of the burner were varied, the modeling provided data on general properties of the flame and flows, as well as spatial distribution and production of carbon monoxide (CO), nitrogen oxides (NO_x), and formaldehyde.

1.2. Anatomy of a Range-Top Burner Flame

In the typical residential range-top burner, flames issue from ports arranged on the circumference of a disk of diameter ranging from 5–10 centimeters (cm). Appliances commonly have multiple port sizes and show variation in the arrangement, size, and shape of ports. Port sizes generally vary from 0.5 millimeters (mm) to 2 mm. Interior to the burner (i.e., within the disk mechanism), natural gas enters from the supply, entrains and mixes with some air (called *primary air*), and issues horizontally from each port, where it subsequently burns. The mixture velocity is generally not high enough to cause significant turbulence, and visually the flame has a smooth, laminar appearance. This fuel-air mixture is rich; i.e., there is not sufficient oxygen in the primary air to consume all the fuel. After issuing from the port, the flame encounters additional air from the open atmosphere (called *secondary air*) and combustion is completed.

Figure 1: A cooking-range flame.

If the fuel-air mixture issuing from the port would contain exactly the right amount of air (stoichiometric mixture) or excess air (lean mixture), the flame would be classified as a *pre-mixed flame;* these flames use only primary air, no secondary air. As the mixture would emerge from the port it would spread out spatially, its streamlines would diverge, and the velocity of the flow would decrease as a result of the spreading. The flame front would situate itself on the envelope where the laminar flame speed (S_L) and the mixture flow velocity were equal and opposite. The flame front would appear stationary, much as a pedestrian on an airport walkway walking in the wrong direction appears to be stationary to an outside observer if her speed matches that of the walkway. If there existed no such envelope, then a stable flame would not be sustained. For example if the flow velocity were too high everywhere, then the flame would lift and extinguish. If the flow velocity were too low, then the flame would burn into the port. It

is worth noting that S_L depends on both fuel type and stoichiometry. For example, S_L of a stoichiometric methane-air mixture is approximately 40 centimeters per second (cm/s); whereas S_L of a stoichiometric hydrogen-air mixture is approximately 200 cm/s. Generally S_L peaks at mixtures slightly to the rich side of stoichiometric (Jomaas et al. 2005), i.e. when there is not quite enough air to burn all the fuel. As the fuel air mixture moves away from this point – either getting more fuel rich or first moving to stoichiometry then to fuel lean conditions – the flame speed (S_L) decreases. Had the mixture contained no primary air, i.e., only fuel, then the flame is known as a *non-premixed flame*, or *diffusion flame,* as diffusion is the dominant mechanism for supplying air and fuel to the flame front. Non-premixed flames have different geometry (are generally longer) than premixed flames, and they are more sensitive to the geometry of the surroundings and the supply of secondary air. As in the case of pre-mixed flames, its streamlines would diverge and the velocity of the flow would decrease as a result of the spreading.

The mixture used in range-top burners is partially premixed and has properties of both premixed and non-premixed flames. A closer look at Figure 1 reveals an inner premixed flame front and an outer diffusion flame, just as one sees in Bunsen flames.

Even for such a simple laminar premixed flame there is more than meets the eye. Some of the multiple processes simultaneously occurring are:

- Chemical reactions
    - Fuel and oxygen are consumed.
    - Intermediate radicals are formed.
    - Final burnt products and pollutants are formed.
    - Enthalpy (i.e., heat) is produced.
- Heat conduction
    - Heat from the flame zone is conducted forward where it pre-heats the fuel and also enhances radical production.
- Convection
    - Bulk movement of gas is propelled by the existing momentum of the fuel and oxidant issuing from the port.
    - Turbulence aids in additional mixing of fuel with secondary air.
    - The burnt gases expand.
    - Buoyancy of hot gases removes burnt products from the flame region and causes flame to incline upward.
- Diffusion, the movement of molecules by random motion (Brownian motion) from areas of higher to lower concentration

    - Molecules of the light radicals move ahead of the flame into the fuel, where they help to initiate and perpetuate the flame.
    - Oxygen from the open atmosphere diffuses into the flame, providing the secondary air necessary for complete combustion.
- Radiation, which generally serves to remove heat energy from the flame region. In non-sooting flames, radiation is emitted directly from hot gas molecules. In sooting flames, radiation is also emitted from incandescent soot particles, giving the flame the familiar yellow color.

These physical and chemical processes are represented by mathematical equations. Numerical forms of these equations are implemented in computer programs to simulate combustion under various conditions of interest.

1.3. Computational Modeling of Flames

The advent and availability of computers in the 1970s spurred the development of the fields of Computational Fluid Dynamics (CFD) and computational chemical kinetics, which naturally led to a marriage of the two, permitting computer simulation of combustion.

The approach is to discretize the physical domain of the flame in space and in time. The physical one-, two-, or three-dimensional) domain of the problem is represented by a grid composed of adjacent cells. In each cell an initial temperature, pressure, velocity, and mixture of gaseous chemical species are specified. Starting from an initial time, the state of the system is then advanced in discrete time steps.

At every time step the physical processes referred to in Section 1.2 are simulated by means of partial differential equations for diffusion, convection, conduction, and other conditions. These simulations provide velocity, pressure, convection across cell boundaries, the equation of state, turbulence, and the diffusion of chemical species across cell boundaries. At every time step the chemical processes mentioned in Section 1.2 are solved by means of a system of ordinary differential equations that describe the chemical reactions. Chemical equations are solved for each cell independently, and for that cell, determine the changes in concentration of each chemical species and enthalpy at every time step. Chemistry is modeled through use of a chemical mechanism that specifies reactions and reaction rates for a suite of chemical species that includes reactants, products, and intermediate species. Even supposedly simple combustion such as hydrogen burning in air (which is commonly thought of as simply $2H_2 + O_2 \rightarrow 2H_2O$) requires a mechanism with 8 chemical species and 26 reactions. A well-known methane combustion mechanism, GRI-Mech, (Frenklach et al. 1995) has 53 species and 325 reactions, and a heptane combustion mechanism (Curran et al. 1998) has 544 species and 2446 reactions! The chemistry portion of the calculation frequently proves to be more computationally demanding than the CFD portion, depending on the size of the reaction set and the method of solution. In this author's experience the hydrogen chemistry used 80% of the computer time, while methane combustion used more than 95%.

Grid resolution (i.e., the cell size) is very important to capture the features of the flame, and also to produce an accurate result. The size of the time step must be restricted to be smaller than the timescales of the physical and chemical processes that are occurring. While for accuracy it is generally desirable to use smaller grid cells and smaller time steps, a penalty is paid in the computational cost. For example decreasing the cell size by ×2 in a 3-D grid approximately increases the number of cells by 2^3. Since the mathematics of the solution method requires that the time step also be decreased by ×2, we find that improving our grid resolution by ×2 increases the computational cost by ×16.

In addition to calculations within the grid, calculations are required on the boundaries. Some boundaries are inflows and outflows, and require specification of gas mixtures, temperatures, and pressures external to the boundary. Other boundaries are solid; for these the degree of drag and thermal conduction between the gas mixture and the solid wall must be calculated.

The output of a calculation generally consists of the pressure, temperature, density, velocity, and chemical species concentrations for every cell in the grid. Depending on the focus of the study in question, it may include other quantities of interest such as turbulent kinetic energy, species fluxes between cells, time derivatives of the above-mentioned quantities, or radiative heat flux.

2.0 Methods

2.1. Overview

This section covers the details of the modeling approach, the modeling software, grid setup, analysis software, chemical mechanism, and a brief qualitative description of a typical simulation run.

2.2. General Simulation Plan

Multiple simulations were conducted, during which the gas composition of the fuel, flow rate of the fuel-air flow and equivalence ratio[1] of the f**u**el-air flow were varied. All simulations used the 3-D gridded reactive computational fluid dynamics (CFD) code Kiva (Torres and Trujillo 2006) to simulate the gas flows and chemical reactions within natural gas flame. The grid represented a single port of the burner. The partially premixed fuel-air mixture issuing from the port fueled a laminar flame with both premixed flame and non-premixed flame regimes. A simulation was continued until the flame achieved a steady appearance, and the state of the flame at this final time step was used for subsequent analysis.

2.2.1. Selection of Gas Compositions

The gas compositions were selected from among the mixtures used in LBNL's Task 9 experimental measurements, with three gases ultimately chosen: Baseline Gas, Gas 3A, and Gas 3C. For the simulations, the small fraction of butane (C_4H_{10}) in these mixtures has been shifted to propane, since the chemical mechanism includes species containing up to three carbon atoms. The mechanisms get exponentially more complicated as the number of carbon atoms increase.

Table 1: The three gas mixtures used for simulations, showing fractional composition by volume of methane, ethane and propane in the fuel.

Gas Label	Methane (CH_4) (%)	Ethane (C_2H_6) (%)	Propane (C_3H_8) (%)	Wobbe Number	Heating Value (KJ/mole)
Baseline	96.72	2.70	0.58	1336	917
3A	90.2	5.77	4.03	1417	983
3C	86.46	11.97	1.57	1419	992

KJ = kilojoules

The composition of air by volume in all simulations is 78.1% nitrogen (N_2), 20.9% oxygen (O_2), 0.93% argon (Ar), 0.03% CO_2, and 10^{-4}% water (H_2O) unless otherwise specified.

[1] *Equivalence ratio* (denoted by ϕ) measures the relative proportions of fuel and oxygen in the unburned mixture. $\phi=1$ (stoichiometric mixture) indicates that there is exactly enough oxygen to consume all the fuel. $\phi>1$ (rich mixture) indicates that there is insufficient oxygen to consume all the fuel. $\phi<1$ (lean mixture) indicates an excess of oxygen.

2.2.2. Choice of Flow Rates and Equivalence Ratios (ϕ)

In residential range-top burners only the fuel flow rate can be controlled. Within the burner mechanism the flowing gas passively entrains and mixes with some air before issuing from the ports. The degree of entrainment of this primary air depends on the flow rate and the internal geometry of the burner; therefore, these two quantities are not independent of each other, and a plot of flow rate versus ϕ for a particular appliance appears as a curve. In the absence of such experimentally determined curves for commercial appliances, this analysis used data from a study conducted by the Gas Technology Institute (Johnson and Rue 2003). In this study a non-commercial research device, the T1 burner, independently varied the primary air fraction and flow velocity for several single-component fuels (CH_4, ethylene (C_2H_4), C_3H_8). The limits imposed by lift-off and yellow-tipping were determined. *Lift-off* occurs when the flow velocity is so high that there is no envelope at which the laminar flame velocity can match it, therefore the flame is pushed back and extinguished. *Yellow-tipping* occurs as the inflow though the port is made richer, resulting in the formation of soot particles, which glow incandescently. The area between the various curves indicates where a non-sooting blue gas flame can be sustained without yellow-tipping or lift-off.

We used these results to select a range of flow velocity and ϕ between the lift-off and yellow-tipping limits. These limits are shown in Figure 2 with the data transformed from GTI's variables thousand British thermal units per hour per square inch (MBtu/hr/in^2) and Percentage Primary Air (see GTI report, Figure 5.3) to variables more directly useful for our simulations, namely, flow velocity and ϕ. Keeping ϕ constant and increasing inflow velocity ultimately leads to flame lift-off (blue curve). Keeping inflow velocity constant and decreasing the fraction of primary air increases ϕ, leads to yellow tipping (red curve) associated with soot formation. A third limit that bears consideration is *blowback,* a condition in which the flame travels back down the port. This occurs when the flow velocity is less than the laminar flame speed (S_L). The black curve at bottom left of Figure 2 is the S_L for methane laminar flames, and indicates where blowback would occur.

To confirm the validity of this regime of flow velocity and ϕ, the flame heights and heat-release rates from preliminary simulations were compared against observed values and specifications for a residential burner described in Appendix A. For this analysis, we used a five point design (green asterisks on Figure 2) to examine variations in flow velocity and ϕ. The boundary design values for flow rate were 0.75 meters per second (m/s) and 1.25 m/s, and for ϕ were 2 and 3. The central point was at flow rate = 1 m/s, ϕ = 2.5. This simulates operation at medium cooking range output, where most cooking occurs. Simulations were conducted with these five conditions and baseline gas to explore the variation of pollutants and flame properties as flow rate and ϕ are changed. The central design point alone was then used to explore the effect of changing gas composition.

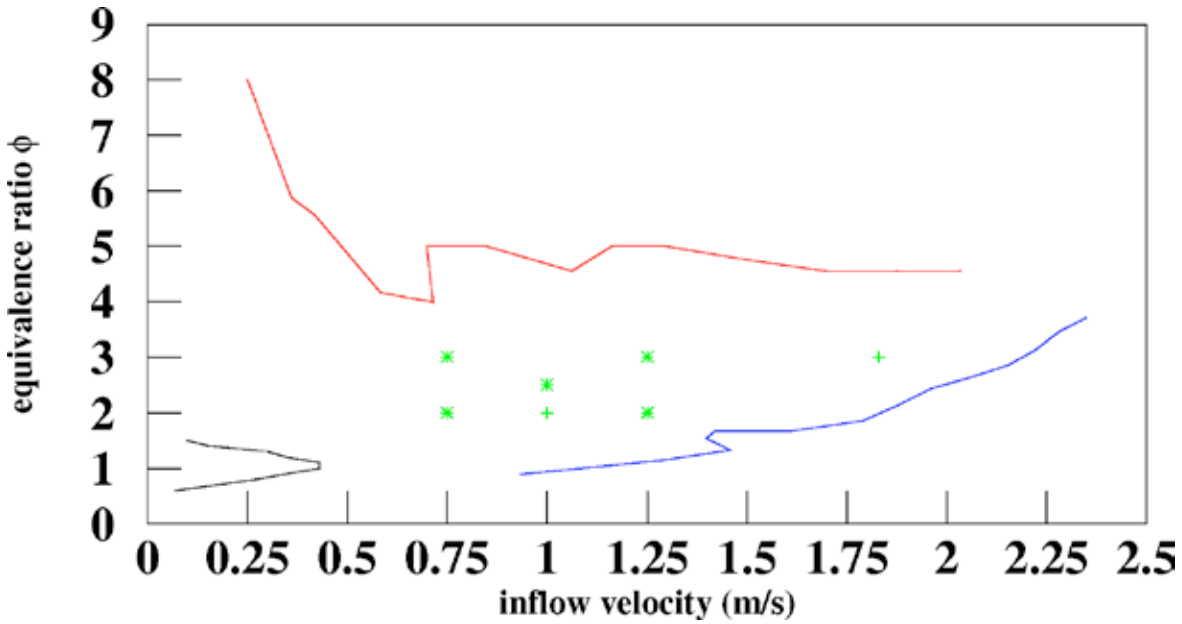

Figure 2: Limit curves of lift-off (blue), yellow-tipping (red), and blowback (black) for a CH_4 flame.

The five-point design (green asterisks) and two additional simulations (green + signs) are indicated.

Two additional design points (green "+" signs on Figure 2) are presented. The condition of v = 1 m/s, ϕ = 2 was simulated based on an earlier plan, and the point at far right (v = 1.84 m/s, ϕ = 3) was subsequently added to simulate a high heat-release case of maximum output (see Appendix A). The latter point has considerably higher energy delivery (38 MBtu/hr/in^2) than the central design point (17 MBtu/hr/in^2). All three of the gas mixtures were investigated at this high heat release condition.

2.3. Modeling Procedure with the Kiva Reactive CFD Software

The Kiva software was developed at Los Alamos National Laboratory in the late 1980s, and has evolved over the years with new version releases every few years. For this study, Kiva 4 was purchased from the Energy Science and Technology Software Center, a Division of the Office of Scientific and Technical Information (OSTI) based at Oak Ridge National Laboratory. It was initially installed and tested on a Centos Linux desktop system, and later ported to a 56 processor parallel Linux cluster at LBNL.

2.3.1. Preparatory Setup, Code Modifications, and Quality Assurance

Prior to starting on the main set of simulation, the modeling code and chemical mechanism were tested under simplified conditions, debugging tools were developed, and appropriate values for the operational parameters of the modeling code were determined. Initial tests using simplified grids and simplified chemical mechanisms were conducted, interfaces were written to enable Kiva output to be read by visualization and analysis software, and necessary code modifications to Kiva and Kiva's grid generator program were made. Single-cell and one-dimensional (1-D) grids are essential for testing within minutes whether changes made to

computer code work as desired. They also verify that a chemical mechanism is performing reasonably in a simplified environment without the confounding CFD influences.

2.3.1.1. *Simplified Single-Cell and One-Dimensional Grids*

A single-cell grid was used to test the interface to the chemistry package Chemkin (described in Section 2.3.1.2), comparing calorimetry and different enthalpy tables used in Chemkin and those built into Kiva. It was also used to compare the same mechanisms within the Kiva and another similar CFD code, Coyote (Cloutman 1990), as a further check.

A one-dimensional grid (Figure 3) was used for fast tests (several minutes on a desktop computer) of the chemical mechanism, gas-mixtures, fuel-air stoichiometry, graphics interfaces, and code modifications. The left and right boundaries of this grid were open. A fuel-air mixture at 300 Kelvin (K) flowed into the right boundary; the left boundary was an outflow with air at temperature T = 300 K, pressure P = 1 atmosphere outside. Within the grid the (laminar) flame burned into the inflowing mixture. Walls were free-slip and adiabatic. No turbulence model was used. Figure 3 shows a temperature field in this 1-D grid.

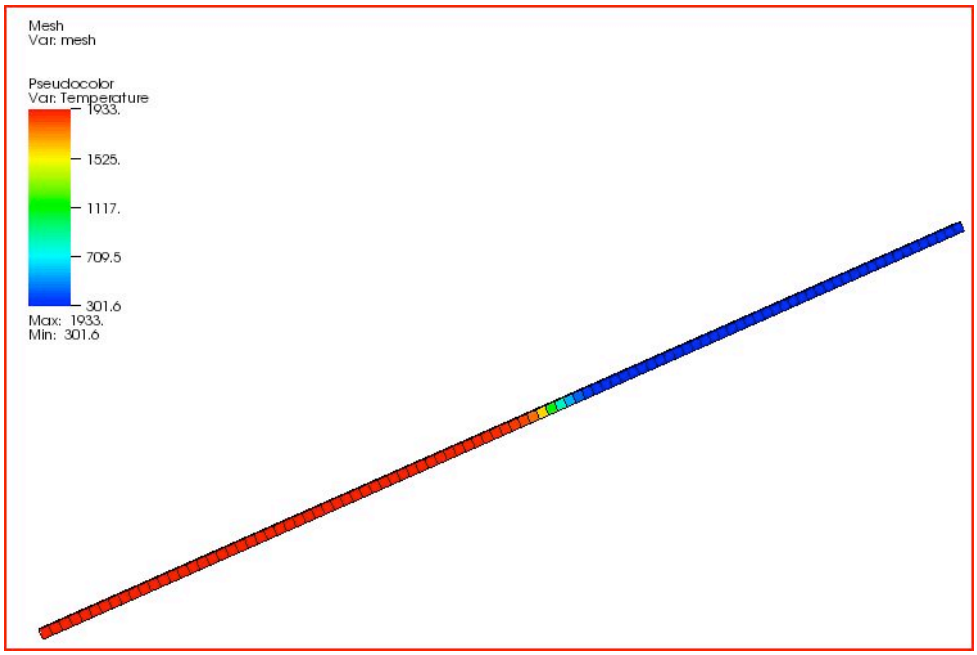

Figure 3: 1-D (100x1x1 cells) grid for testing. The 1 cm long domain is divided into 100 cells.

2.3.1.2. *Interfaces to Other Software*

To analyze Kiva gridded output, interface subroutines to the Chemkin II chemical kinetics package and to several graphical analysis packages were written and embedded in the Kiva code.

1. **Chemkin/DVODE Interface:** The original Kiva pre-dated the Chemkin chemical kinetic library (Kee et al. 1996) and DVODE stiff Ordinary Differential Equation solver (Brown

et al. 1988) used to integrate the chemical reaction rates. Over the years these have never officially been incorporated into Kiva. Since the Chemkin format is the most widely accepted format for chemical mechanisms, Chemkin and DVODE were interfaced into Kiva.

2. **PAW (**Physics Analysis Workstation) from CERN provides a structured query language (SQL)-like interface for simulation output data to be queried and interrogated very precisely and viewed in histograms and multi-dimensional scatter plots (Brun 2010).

3. **GMViewer:** The General Mesh Viewer software package from Los Alamos National Laboratory was crucial during the grid construction stage (Ortega 2010).

4. **VisIt** package (Childs et al. 2005) from Lawrence Livermore National Laboratory is a free, open-source, Python-based package, currently (as of early 2011) very actively supported. VisIt has data interrogation and visualization capability, and support for a large number of input data formats. A VisIt interface to Kiva was written to produce Silo output, the preferred native format of VisIt.

2.3.1.3. *Code Modifications*

The following major modifications were made:

1. **Reprogramming of the advective flux subroutine** so that distinct mixtures are allowed on different inflow boundaries. Our domain requires a partially premixed fuel-air mixture through a port and an air inflow from the bottom boundary.

2. **Reprogramming of the subroutine which handles gravitational forces** so that the hot burnt mixture feels the correct buoyant force.

3. **Parallel programming:** The 3-D grid and large chemical mechanism being considered required more computational resource than could be supplied by a desktop computer. Accordingly, LBNL generously made parallel computing resources available. (A Beowulf Linux cluster ≈ 6 years old, with 42 processor elements, or PEs.) While parallelization of a CFD code often requires partitioning of the grid and assigning the partitions to different PEs, and is a lengthy process, we invoked a simpler method in which only the chemistry is parallelized. This was a workable solution because with large chemical mechanisms most of the computational burden occurred within the chemistry module. The chemistry calculations were contained within each cell, with no inter-cell communication required, unlike the calculations for other physical processes. In the simplified parallelism implemented for this project, a master PE did all of the CFD calculations and then farmed out the chemistry calculations to the other PEs. A load-balancing algorithm ensured that the PEs were all assigned the same workload; particularly important since some portions of the grid had little or no chemistry, while other portions, such as hot regions near the flame front, had extensive chemistry. Additionally some of the PEs were several years older, and therefore slower, than others. Dr. Tonse parallelized the CFD code Coyote, from Lawrence Livermore National Laboratory (LLNL) in a similar way in the late 1990s; much of that code was reused here

and upgraded to make it more efficient. With the new parallel code and the Linux cluster, a full simulation takes four to seven days to complete with 10–20 PEs.

4. **Radiation model:** A radiation model, adapted from the Coyote code was added to Kiva. Radiative emission by Stefan-Boltzmann's law for H_2O, CO_2, and CO was calculated using their Planck mean opacities. These species were selected as the high concentration species with non-zero electric dipole moments that were present in high-temperature parts of the flame. Radiation transfer was not calculated; i.e., once radiation was emitted, it left the system. The effect of removing radiated energy by this model reduced peak flame temperature by less than 20 Kelvin.

5. **Non-uniform grid:** The grid generator supplied with Kiva produced grid cells of uniform size. The code was modified so that grids with varying cell size could be generated (discussed later in Section 2.3.2.3).

2.3.2. Three-Dimensional Grids

2.3.2.1. *Grid Description and Dimensions*

The modeling domain was represented by a rectangular Cartesian grid with an inflow port on the right wall, to simulate a single port. The x-axis represents the horizontal dimension in line with the burner port, starting from a zero point beyond the flow impacts of the flame and positive values moving toward the burner. The y-axis represents the horizontal dimension perpendicular to the burner port, with positive values moving away from the observer. The z-axis represents the vertical dimension, with zero set at the centerline of the port. We refer to the X boundaries as "left" and "right," Y as "front" and "back," and Z as "top" and "bottom." The origin was at the left-front-bottom corner. The grid dimensions were: X = 3 cm plus 0.5 cm for the port, Y = 2 cm, and Z = 3 to 6 cm, where Z varies from 3 to 6 cm as various sizes were tried. The port was 0.5 cm long in X and 0.2 cm wide in both Y and Z. The center of the port's left face intersected the right wall at coordinate (3.0 cm, 1.0 cm, 1.0 cm). The choice of port diameter and port spacing was based on the CT03 burner used in the LBNL Task 9 experimental measurements (Singer et al. 2009) and the Range 2 burner of the GTI Gas Interchangeability study (Johnson and Rue 2003). Both of these are manufactured by Maytag, and from photographs appear very similar. In these burners, the port diameter was 0.19 cm (0.075 in) with 0.6 cm spacing between ports.

Chronologically, after completion of many of the simulations, it was realized that our specification of a 0.5 cm port length was larger than in most residential range-top burners. The port length should correspond to the thickness of metal used in the outer rim of the disk from which the mixture of gas and air issues and is likely 0.1–0.2 cm. This difference may have consequences on the profile of the velocity entering the main grid from the port since viscous drag of the gas flow on the port wall would cause the profile to have a more parabolic shape for the longer port. Accordingly simulations with port lengths of 0.1 cm and 0.5 cm were compared (Section 3.5). Differences were seen between the two cases, but not sufficiently to change the conclusions. The final set of simulations, involving high heat release, was conducted with this 0.1 cm port length.

2.3.2.2. *Boundary Conditions*

The setup of boundaries involves making decisions on whether each open boundary at a grid edge is to be inflow or outflow. The port itself is obviously inflow. The inflow port is on the right wall, and a partially pre-mixed fuel air mixture flows toward the left, into the main domain. Air inflow also occurs from the bottom. Burnt gases flow out of the top and left walls. The front and back walls are solid.

In addition to calculations within the grid, calculations are required on the boundaries. Both inflow and outflow boundaries require specification of gas mixtures, temperatures, and pressures external to the boundary. For solid boundaries the degree of drag and thermal conduction between the gas mixture and the solid wall must be specified.

To reproduce the geometry of an actual burner, the right wall is solid below the port and for the first 0.5 cm above it; above that it is an open boundary set to be a pressure inflow boundary with unburned air outside. For this boundary it is debatable whether it is more appropriate to use unburned air or burnt air coming from another flame. In a real device, the neighboring flames would restrict the lateral spread of the flame. Since this analysis simulated only a single flame, an attempt was made to mimic the restrictive effect of the neighboring flames by setting the front and back boundaries as solid. The following bullets summarize the boundary conditions (BC) (see the color-coding in Figure 4):

- Left: Specified-Pressure Outflow BC.
- Right: Solid below and immediately above port. Pressure inflow above that.
- Port: Rectangular Specified-Velocity inflow BC.
- Front: Solid.
- Back: Solid.
- Top: Specified-Pressure Outflow BC.
- Bottom: Specified-Pressure Inflow BC.
- Unless otherwise specified the mixture outside open boundaries is air at P = 1 atmosphere (atm) and T = 300 K.
- The Specified-Velocity inflow BC at the port is at T = 300 K also.
- All walls are adiabatic.
- The drag on walls is discussed in Section 2.3.3.2 (Wall BC).

2.3.2.3. *Grid Resolution*

Grid resolution (i.e., the cell size) is very important to capture the features of the flame, and also to produce an accurate result. While for accuracy it is generally desirable to use smaller grid

cells and smaller time steps, a penalty is paid in the computational cost. Decreasing the cell size by ×2 in a 3-D grid approximately increases the number of cells by 2^3.

Initially a uniform grid with 1 mm cubic cells was constructed and tested with a CH_4 fuel and the 21-species DRM-19 methane mechanism. After early simulations it became apparent from the flame appearance that this resolution was insufficient. The cell size was reduced to 0.5 mm per side, which increased the number of cells from 36,000 to 288,000. While this resolution was sufficient, the large number of cells made the computational time very large with the USC C3 mechanism (described later in Section 2.4), even using the parallel Linux cluster. To resolve this, an algorithm was written to stretch the grid in regions where such resolution was unnecessary. The new grid (Figure 4) has 0.5 mm resolution near the port and flame regions, and then geometrically increases cell size with distance from the port. The number of cells is now a more tractable 65,500.

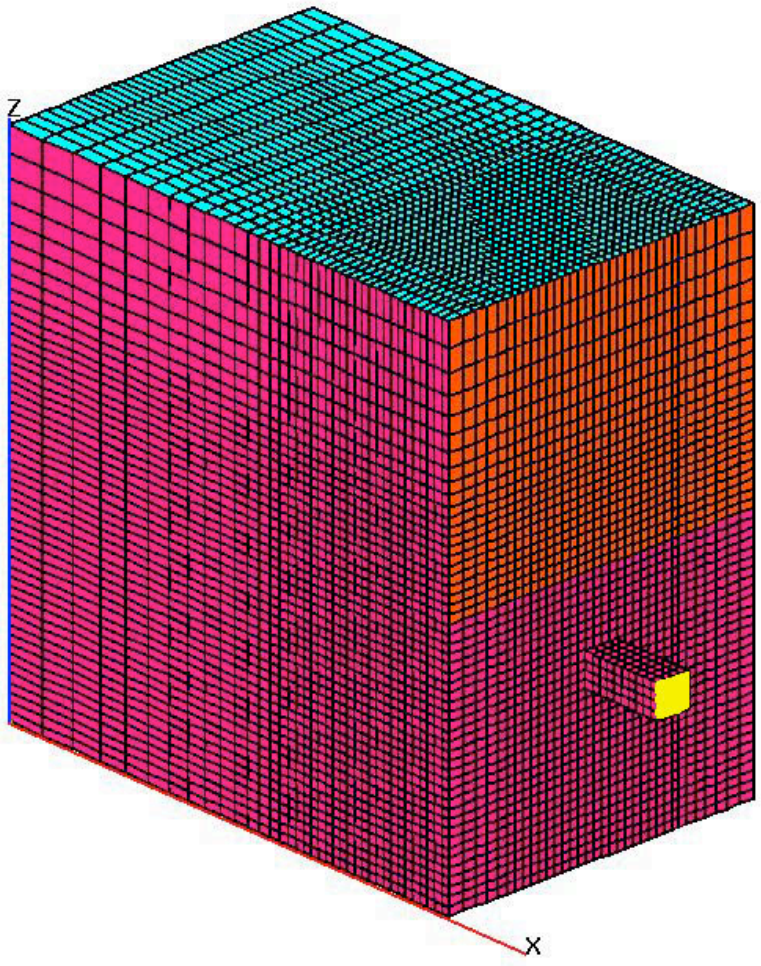

Figure 4: Variable resolution grid used for majority of simulations.

Cell size is constrained to 0.5 mm near the port and then geometrically increases with distance from the port. Boundary conditions applied to Top, Front, Port, and Right faces are: blue=pressure outflow, magenta=solid, yellow=velocity inflow, orange=pressure inflow.

2.3.3. Operational Parameters

Similar to many other CFD software packages, Kiva comes with several "knobs," operational parameters, and sub-model choices. Many of these are pre-set and come with recommended values or ranges, while others are left entirely to user specification.

2.3.3.1. Turbulence Model

Turbulence manifests itself as velocity fluctuations which are often vortex-like in appearance, and which occur at many length scales. Some of these are large enough to be visible in the grid's velocity field, while others have length scales smaller than that of the grid cells. Since these smaller-length scale fluctuations contain turbulent kinetic energy, they cannot simply be ignored. Turbulent kinetic energy and momentum moves from larger scale to smaller scale fluctuations, eventually ending up as heat. Turbulence modeling is the process by which this cascade of kinetic energy is calculated.

Kiva offers three choices of turbulence model: (1) a standard, older, RANS k-ε model, (2) a newer RANS renormalized group model (RNG), and (3) a Large Eddy Simulation (LES) model. In this study's Kiva simulations the turbulence level is not very high, and there are no visible wrinkles or other large features in range-top flames. The low turbulence level is assessed with the Reynolds number, a dimensionless quantity useful for differentiating between laminar and turbulent flows. For this system, a Reynolds number of approximately 100 was estimated, using $\nu_{air} = 0.15\times10^{-4}$ square meters per second ($m^2\,s^{-1}$), U = 1 m s^{-1}, and L = 10^{-3}; where ν is kinematic viscosity, and U and L are approximations of the velocity and length scales of the problem. Therefore the LES choice was considered unnecessary. Between RNG and k-ε, RNG is generally accepted as having better fundamentals and performance. Additionally it was recommended over k-ε by the Kiva developers at Los Alamos National Laboratory (LANL).

2.3.3.2. Wall Boundary Conditions

The wall BC in the inflow pipe influences the flow velocity and turbulent kinetic energy of the inflowing mixture. Wall BC choices in Kiva are (1) free-slip wall (no drag), (2) no-slip wall in which the cell closest to the wall has its tangential velocity zeroed, the tangential velocity profile then evolves based on the stress forces, and (3) LOTW: a parameterized "law of the wall" which uses a turbulent boundary layer treatment (Kiva 2 manual, Appendix B) to apply a tangential velocity profile. While no-slip is the most physically fundamental choice, to implement it accurately requires a sufficient number of cell layers adjacent to the wall. This makes it unsuitable, since within the port there is not sufficient gird resolution to apply it: even with 0.5 mm cells the port is only 4x4 cells in cross-section. A no-slip condition would cause the inflowing gas to concentrate into the inner 2x2 cells away from the walls and enter the main grid at too high a velocity—about four times higher than the specified inflow. The benefit gained from increasing the resolution inside the port is probably not worth the computational penalty in the main cavity of the domain. Therefore this option was rejected, and the LOTW option was used.

2.4. Chemical Mechanism

A review of the recent literature (Pillier et al. 2005; Bennett and Smooke 2005; Jomaas et al. 2005; Walsh et al. 2005; Dworkin et al. 2007; Petersen et al. 2007; Qin et al. 2000; Seshadri and Bai 2007; Bhatia et al. 2005) pointed to several fairly detailed chemical mechanisms. These generally had more than 20 but fewer than 100 chemical species, and on the order of several hundred chemical reactions.

1. The USC C3 mechanism optimized for hydrocarbons up to propane (Qin et al. 2000; Jomaas et al. 2005)
2. GRI-Mech 3.0 (Frenklach et al. 1995; Pillier et al. 2005)
3. GRI-Mech 2.11 (Frenklach et al. 1995; Bennett and Smooke 2005; Walsh et al. 2005)
4. The USC C4 mechanism optimized for hydrocarbons up to butane (Wang et al. 2007)
5. The San Diego Mechanism (Cermech) (Williams 2010; Jomaas et al. 2005)

Final selection required the following:

1. Incorporation of ethane and heavier hydrocarbons as fuels.
2. Ability to predict CO, NOx, and formaldehyde reasonably well.
3. Good agreement with data for S_L and species' concentrations.
4. Recent development, (< 10 years) but not too new (> 2 years); i.e., used and accepted by sufficient number of researchers.
5. Computational feasibility with run times not greater than a few days.

Based on a balance of these criteria, the USC C3 mechanism optimized for hydrocarbons up to propane (which has three carbons; hence the "C3" name) was chosen for production running. This contains 71 species and 468 reactions. A third-party evaluation of the mechanism is presented in Jomaas et al. (2005). A C4 mechanism produced by the same research group at University of Southern California (USC) would have provided additional butane fuel capability, but was considered to be too new.

A simplified picture of the oxidation sequence of the three initial fuels methane (CH_4), ethane (C_2H_6), and propane (C_3H_8) in the C3 mechanism shows:

- Methane oxidation proceeds more or less sequentially with repeated abstraction of hydrogen (H):

  $$CH_4 \rightarrow CH_3 \rightarrow CH_2O \rightarrow CHO \rightarrow CO$$

  but also has an ethane-related component caused by combination of

  $$CH_3 + CH_3 \rightarrow C_2H_6$$

- Ethane initially goes primarily to C_2H_5, which then goes to C_2H_4 and so on.

- Propane proceeds through repeated abstraction of H from the propane molecule:

$$C_3H_8 \rightarrow C_3H_7 \rightarrow branching\ mainly\ to\ \frac{C_3H_6 \rightarrow C_2H_4}{C_2H_5 \rightarrow C_2H_6\ or\ C_2H_4}$$

  The branch to C_2H_5 also links it to ethane.

We see that the oxidation paths are intricately linked, as they lead to common shared intermediates. The relevance of this will be more apparent when we present results comparing combustion from the three gas mixtures introduced in Section 2.2.1. For more detail on the oxidation sequence see Dryer (1991).

The C3 mechanism as such contains neither thermal nor prompt NO_X production. We have added thermal NO_X production by including three reactions of the Zeldovich NO_X mechanism shown below, using the Arrhenius parameters from GRI-Mech 3.0.

$$O + N_2 \leftrightarrow NO + N$$

$$N + O_2 \leftrightarrow NO + O$$

$$N + OH \leftrightarrow NO + H$$

The Zeldovich mechanism produces solely nitric oxide (NO). NO_2 is not included as a species in the C3+ Zeldovich mechanism. While the relative ratios of NO and NO_2 are extremely important with regard to anthropogenic ozone production in the atmosphere, there are chemical equilibrium arguments that the NO_2 to NO ratio is small above 1,500 K (Bowman 1991, Sec 3.4). Prompt NO is produced by the reactions of the CH radical with N_2 molecules. There exists no prompt NO mechanism for C3 (and higher) combustion at present; therefore, we have restricted the calculation to thermal NO. More discussion of this is presented with data on NO_X production in Section 3.2.3.

During the course of the study, two additional simpler mechanisms were also used: DRM-19 (Kazakov and Frenklach 2010), which is a reduced version of the methane fuel mechanism GRI-Mech 1.2. DRM-19 provided a means of testing the Chemkin interface with 21 species (19+N_2+Ar) and was useful for testing new grids with a realistic mechanism. An even simpler one-step CH_4 mechanism containing only five chemical species came bundled with Kiva, and was used for grid-testing and debugging.

2.5. Anatomy of a Simulation

A typical production simulation uses the variable resolution grid of Figure 4, the USC C3+Zeldovich chemical mechanism, an inflowing fuel-air mixture at specified stoichiometry and inflow velocity. The simulation commences (t = 0 seconds [s]) with fuel mixture flowing into the main domain, followed shortly after (t = 0.01 s) by a spark of duration 0.01 s. Ignition occurs and the flame gradually settles to a steady appearance (Figure 5). The simulation is terminated when the temperature and species-concentration fields appear steady, which occurs at about t = 0.5 s. All subsequent analysis uses only this final time step. On the parallel Linux cluster with 10 PEs such a simulation takes six days, with 20 PEs it takes four days.

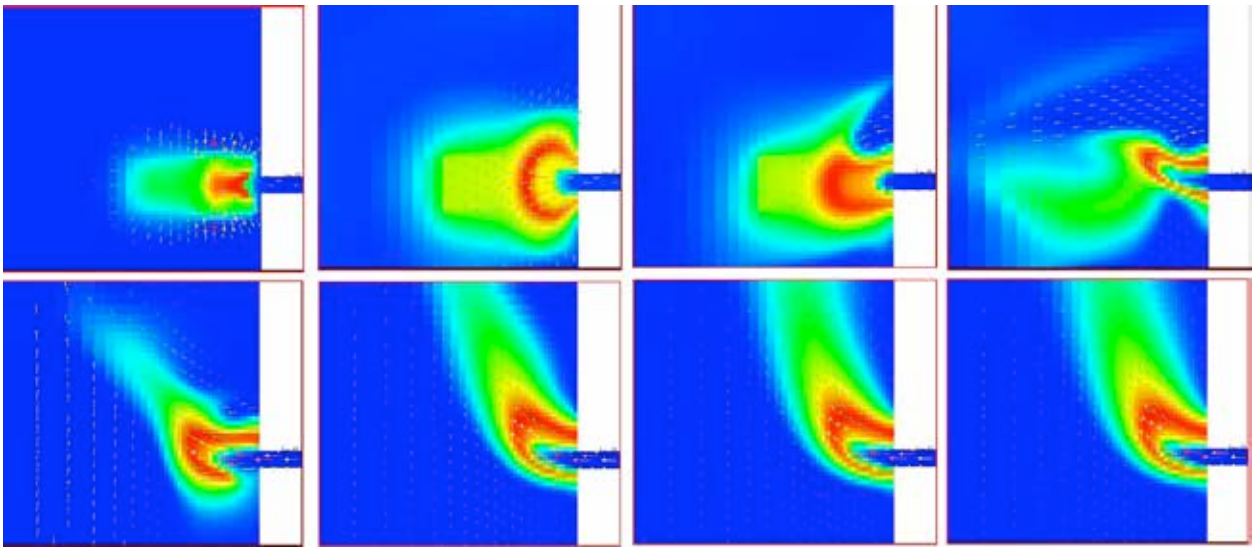

Figure 5: Time evolution of a simulation beginning with sparked ignition, until a steady appearance is attained.

The temperature field (legend not shown) is depicted at times of 0.01, 0.015, 0.017, 0.02, 0.1, 0.2, 0.3, and 0.4 seconds

Generally at this final state the burnt combustion products are exiting from the top, while unburned secondary air enters from the bottom, right, and to a small extent, from the left boundary, although the latter does not reach the flame zone and participate in combustion.

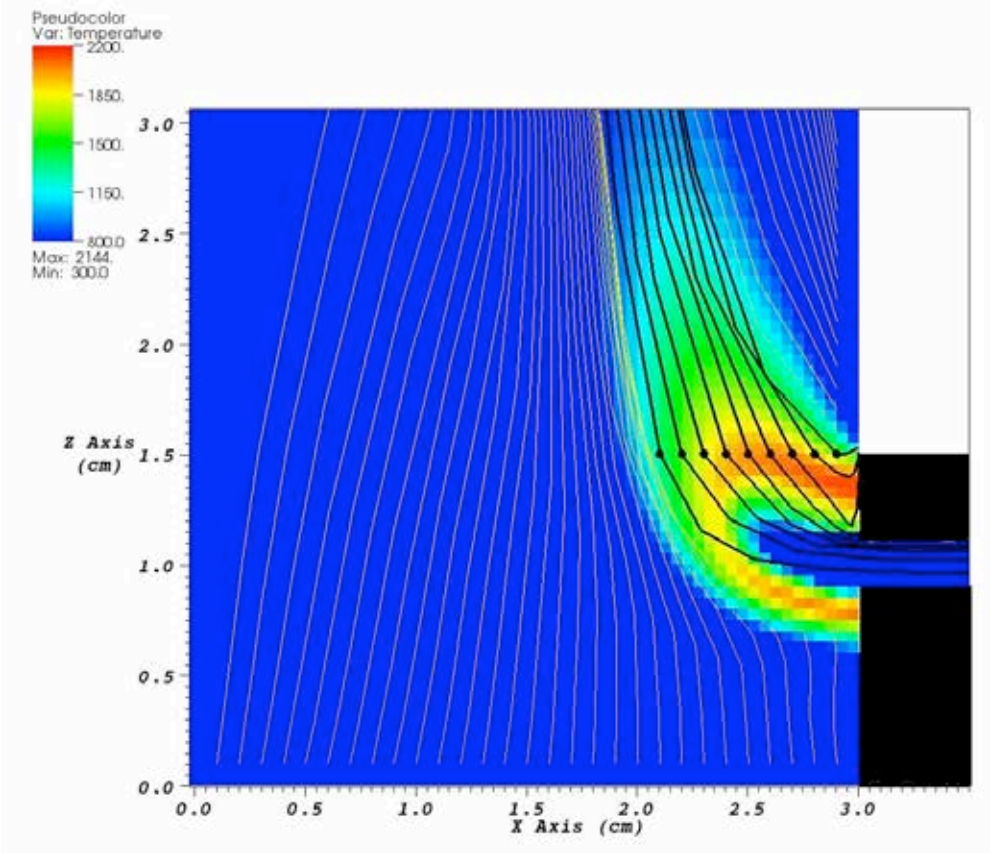

Figure 6: Streamlines indicating incoming fuel and air flows.

The black streamlines show fuel-air mixture from the port, as well as some air from the right boundary entrained in the flame. The black dots are the seed points from which the black streamlines were extrapolated forward and backward. The black solid area surrounding the port is a solid boundary representing the metal of the burner disc. The lighter streamlines show incoming secondary air from the bottom boundary and portion of right boundary above the port.

A depiction of fuel and air flows and their relation to the temperature field can be seen in Figure 6, where the velocity streamlines from the port and the open boundaries have been superimposed on the temperature field.

3.0 Results and Discussion

3.1. Overview

This section begins with presentation and discussion of results for a suite of simulations conducted with the central design point of the baseline fuel. These simulations were conducted to examine the effect of various model design parameters with fuel kept constant. The intent of this initial presentation is to help the reader become familiar with the general features, properties, and details common to all the simulations.

In subsequent subsections, simulation results are presented in the following order: (a) simulations with the baseline fuel mixture, with varying inflow velocity and ϕ (Section 3.3); (b) simulations comparing different fuel mixtures while keeping inflow velocity and ϕ constant (Section 3.4); and (c) other cases, including comparison of simulations that use 0.5 cm and 0.1 cm port lengths (Section 3.5) and a comparison of different fuel mixtures for cases with high heat-release and a 0.1 cm port length (Section 3.6). All simulations in Sections 3.3 and 3.4 use the longer 0.5 cm port length.

3.2. Discussion of the Baseline Gas Central Design Point

3.2.1. Temperature Field and General Flame Properties

The left panel of Figure 7 presents the temperature field with the velocity vectors superimposed, taken at the central vertical slice in the XZ plane (perpendicular to Y axis). This slice goes through the center of the port. Since we specified a 1 m/s inflow velocity into the port, and some compression of the flow into inner cell layers in the port as a consequence of the imposed wall boundary condition, the peak inflow velocity is slightly higher than 1 m/s, but the average velocity is still 1 m/s. Looking head-on at the same flame (Figure 7 right panel), the flame surrounds the incoming fuel-air mixture, with an enlarged hot region immediately above the inlet port.

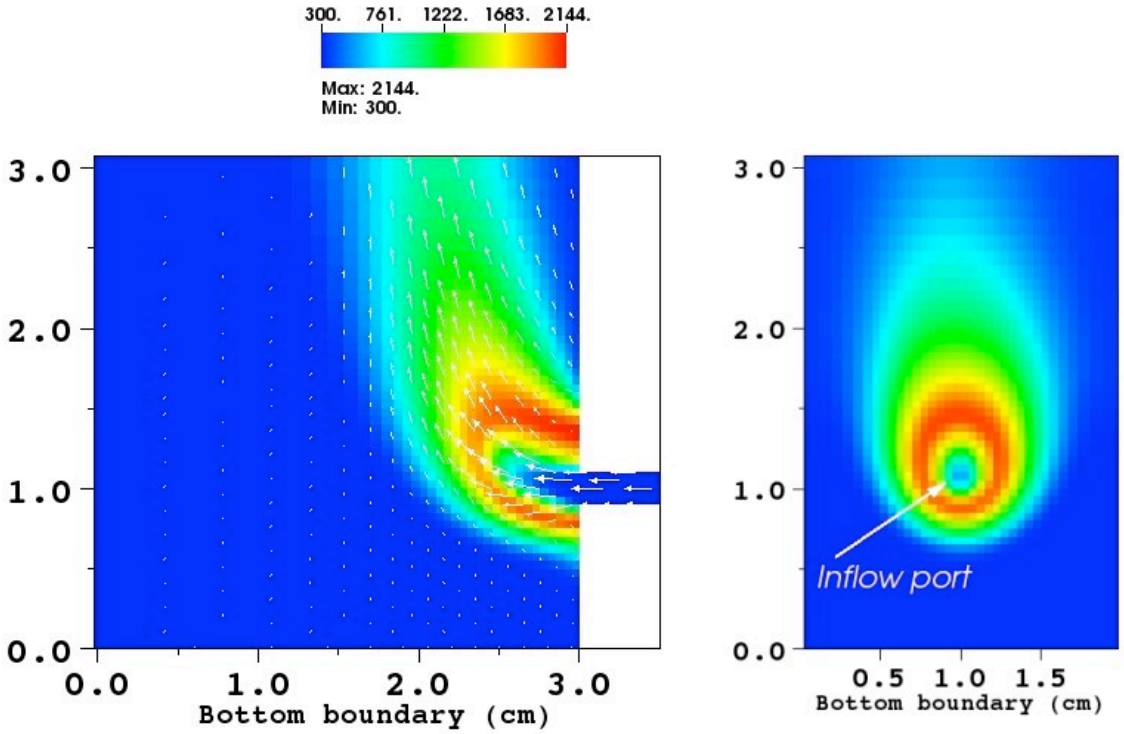

Figure 7: Temperature field.

Left panel: Sliced parallel to the inflow at central Y coordinate. The velocity field is superimposed on this, every fourth vector displayed. Right panel: Sliced perpendicular to the inflow, at x = 2.6 cm; i.e., 0.4 cm from the port orifice.

An additional simulation was conducted to identify regions where premixed and non-premixed burning occurs. To accomplish this, we removed argon from the primary combustion air (issuing from the port) and allowed normal levels of argon in the secondary air entering from the open boundaries. We then tracked the argon/nitrogen ratio. In Figure 8 shows a slice of this ratio normalized so that the normal atmospheric ratio is 1.0. The primary air has a ratio of zero (argon was intentionally removed), while secondary air entering from bottom/sides has the normal atmospheric level. From the gradual change on the plot, the reader can see the extent to which an area is in the premixed or non-premixed combustion zones; e.g., at points where the ratio is 0.75, 75% of the combustion is non-premixed. The shift of some of the nitrogen atoms from N_2 to NO has been accounted for in the calculation of the Ar/N ratio, but that is a small effect.

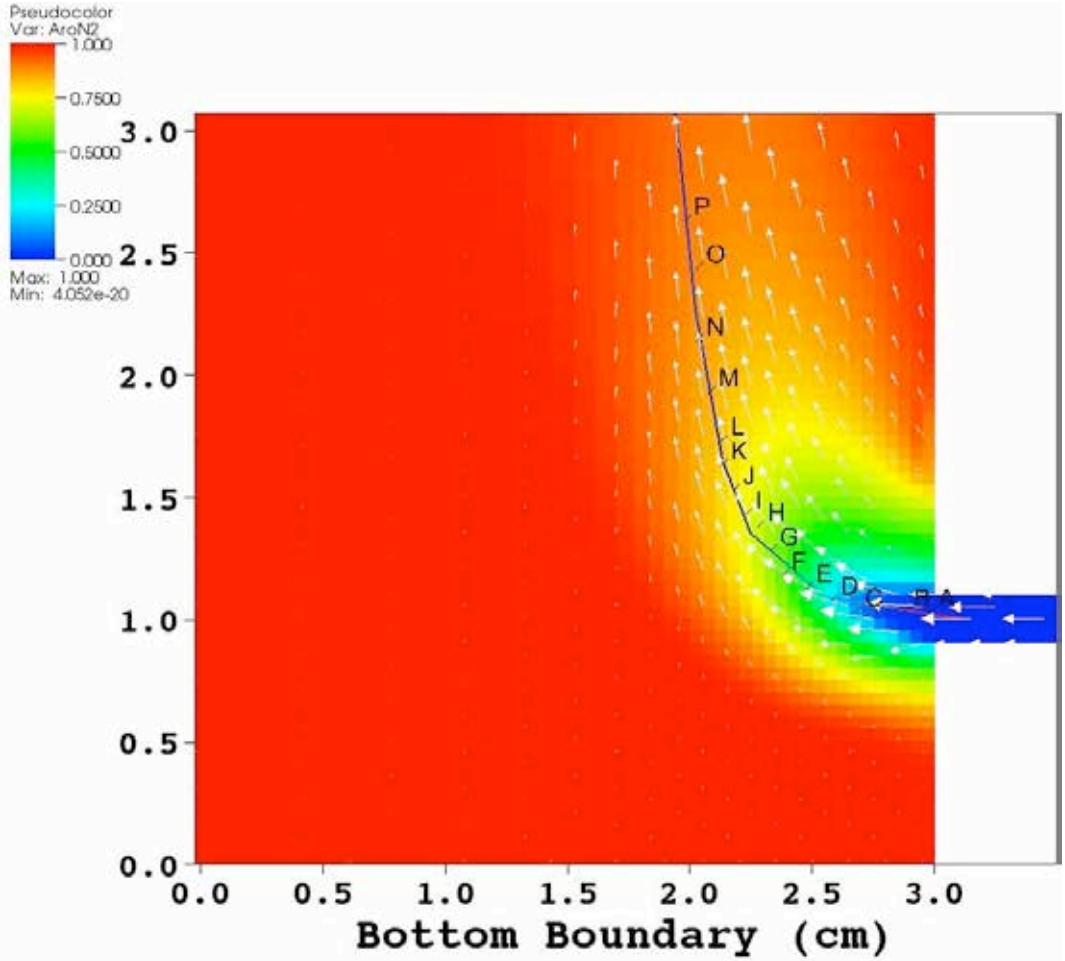

Figure 8: The argon/nitrogen ratio in central Y slice, indicating where premixed and non-premixed combustion occur. Also shown are velocity vectors and a single velocity streamline.

Also indicated on Figure 8 is a single velocity streamline.[2] By using streamlines, a parcel of convected gas can be followed, and in effect its history can be seen. While such an interpretation is helpful in visualizing what happens within the flame, it should be noted that such a parcel is slightly contaminated by diffusion of molecules both in and out.

Along the streamline, several points (labeled A, B, C,…O, P) were hand-picked. In Figure 9 the values of several species and ratios at these points are plotted, using the length dimension of the streamline as an abscissa (x-axis). The streamline passes through the flame zone, and we observe heat release and CO formation, as well as the subsequent oxidation of CO to CO_2. The Ar/N ratio along the streamline is also plotted.

[2] Streamlines are constructed in laminar flows by extrapolating velocity vectors and applying algorithms to determine the most probably path of a flow. A streamline approximately shows the path a light object would take in the flow.

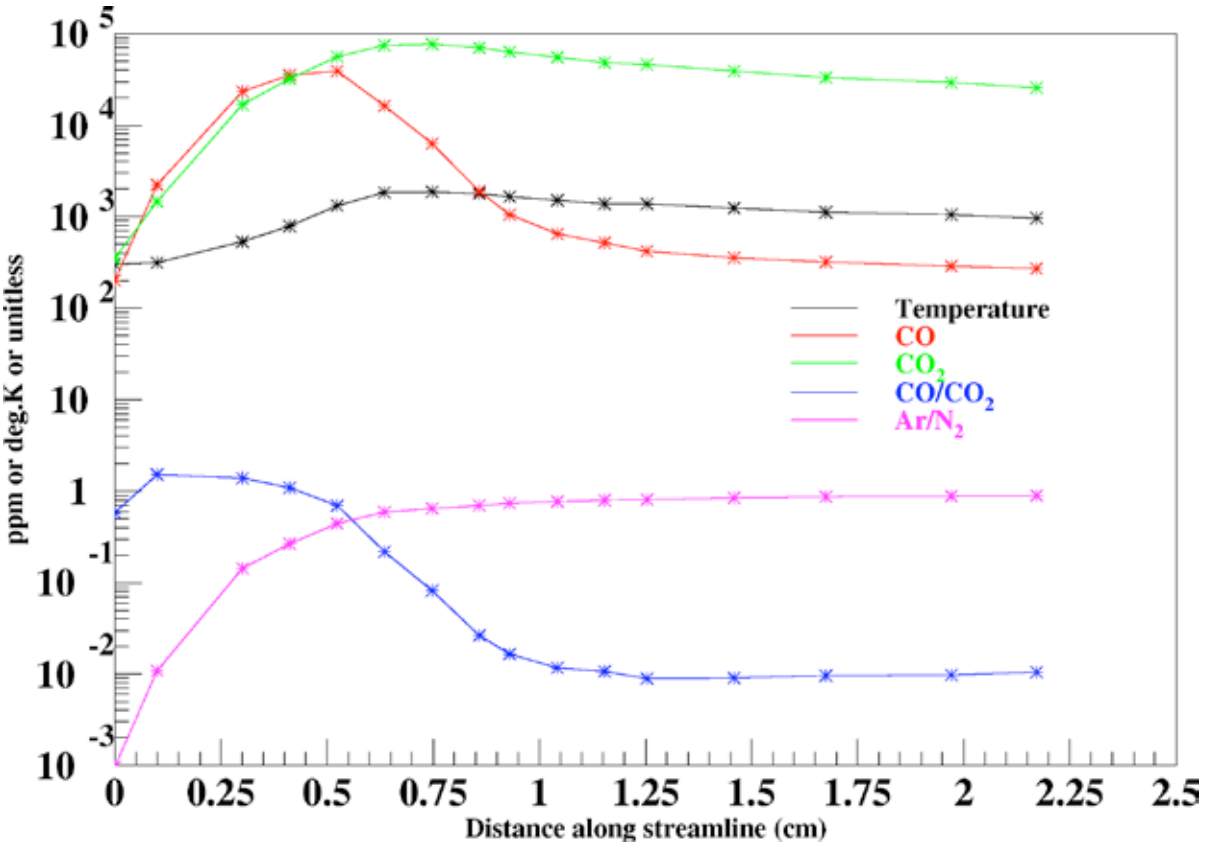

Figure 9: Several quantities plotted at the points selected from the streamline in Figure 8. Y axis units depend on quantity plotted.

The same streamline points are used again in Figure 10 to plot (upper panel) the concentrations of carbon atoms in the fuels, intermediate species, radicals, and oxidation products—in effect following the carbon as it oxidizes. The apparent drop in total carbon in this figure is explained in Section 3.2.2 and Figure 13. The lower panel further classifies the fuels and intermediate species, the intermediate species being sub-classified by the number of carbon atoms per molecule. This is meant to be a rough guide, as there are complications. For example, much C_2H_6 is produced as an intermediate species, but it is also a fuel.

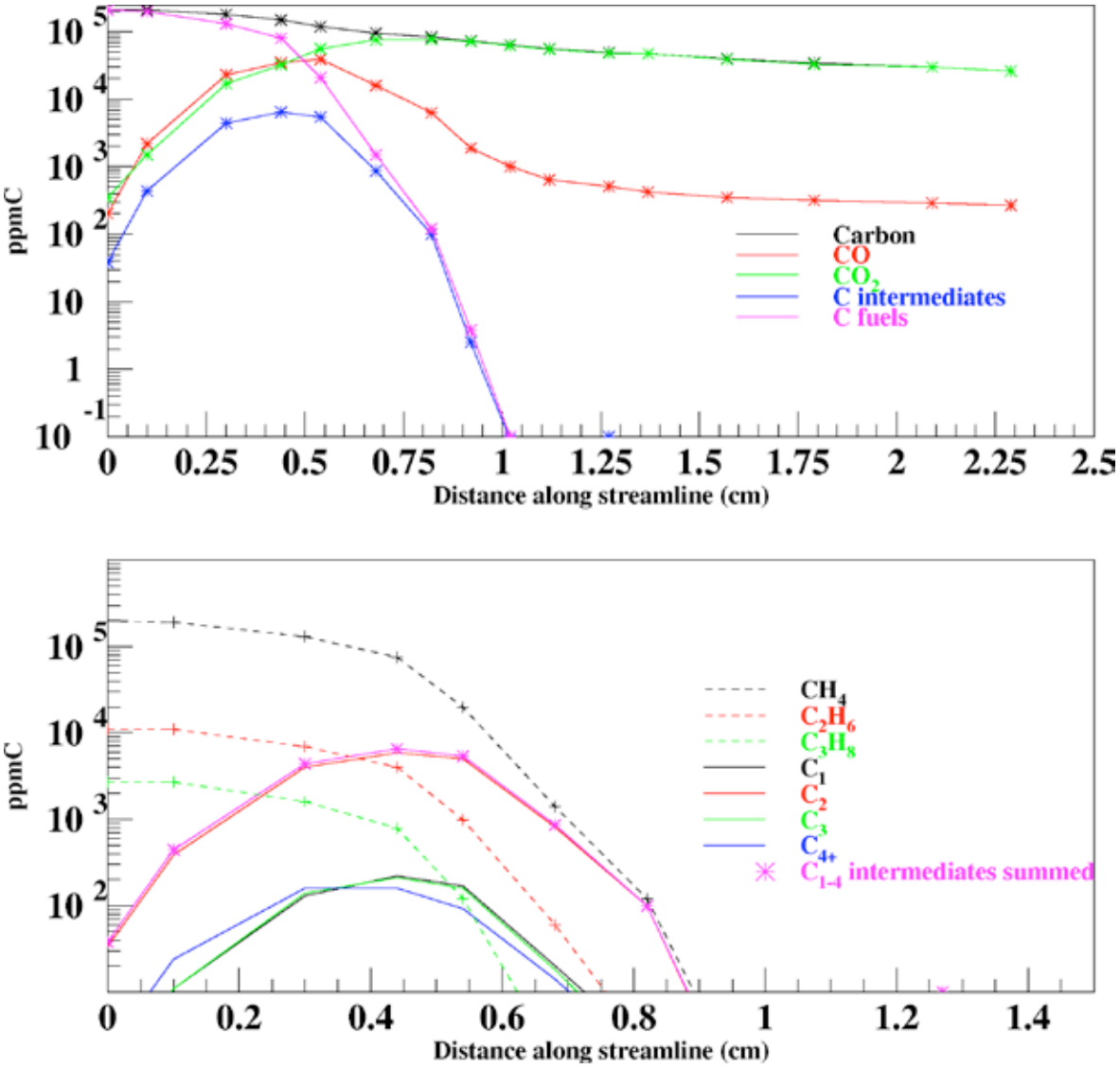

Figure 10: Species concentrations along a streamline.

Top panel: Transfer of carbon from fuels to CO and then CO_2, via carbon-containing intermediate species. Bottom panel: The fuel species and intermediate species are further differentiated. (Note that the top and bottom panels have different scales.)

3.2.2. Carbon Monoxide

Carbon monoxide is a major intermediate during the oxidation of hydrocarbons to CO_2 (Bowman 1991). Within the flame zone CO concentrations can be comparable to those of CO_2, but then decrease sharply post-flame. In the USC C3 mechanism CO forms through several reactions involving CH, formyl radical (HCO), and others. Carbon monoxide is oxidized through reactions $OH+CO \rightarrow CO_2$ and $HO_2+CO \rightarrow CO_2$ and also reactions of CO with O, hydrogen (H_2), and O_2. Figure 11 shows the CO field concentration in parts per million (ppm).

The region of highest concentration (approximately 65,000 ppm) is slightly above the inflow port, similar to the location of highest temperature.

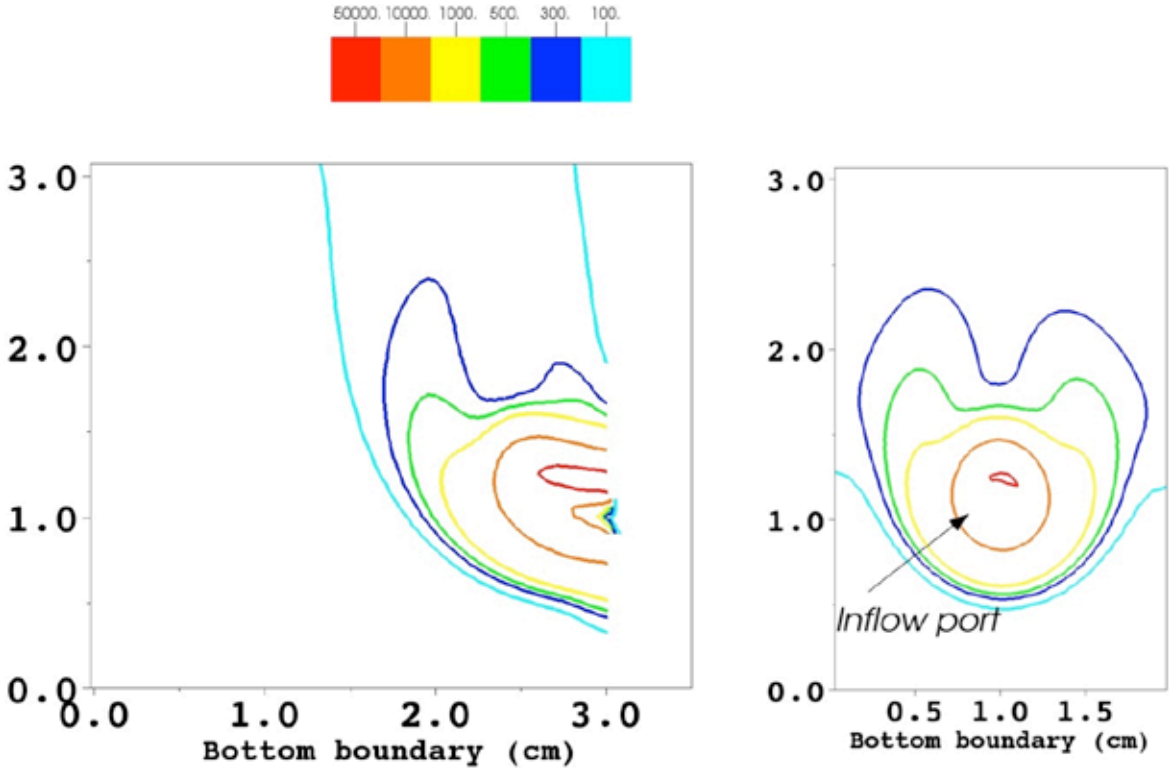

Figure 11: [CO] in ppm (mole fraction × 10^6).

Left panel: Sliced parallel to the inflow at central Y coordinate. Right panel: Sliced perpendicular to the inflow, at x = 2.6 cm; i.e., 0.4 cm from the port orifice, which is centered about (y,z) = (1.0,1.0).

The CO concentration drops not only because of oxidation but also from the lateral spreading of the post-flame region and dilution with outside air. To see the removal of CO by chemical means only, these effects are removed in Figure 12 by summing the CO across horizontal slices (in the XY plane) taken across the entire grid at values of Z every 0.25 cm starting at Z = 1.25 cm. Each slice is one cell layer thick. Note that the x-axis of Figure 12 is used to represent increasing values of Z (i.e., increasing height) of XY horizontal slices.

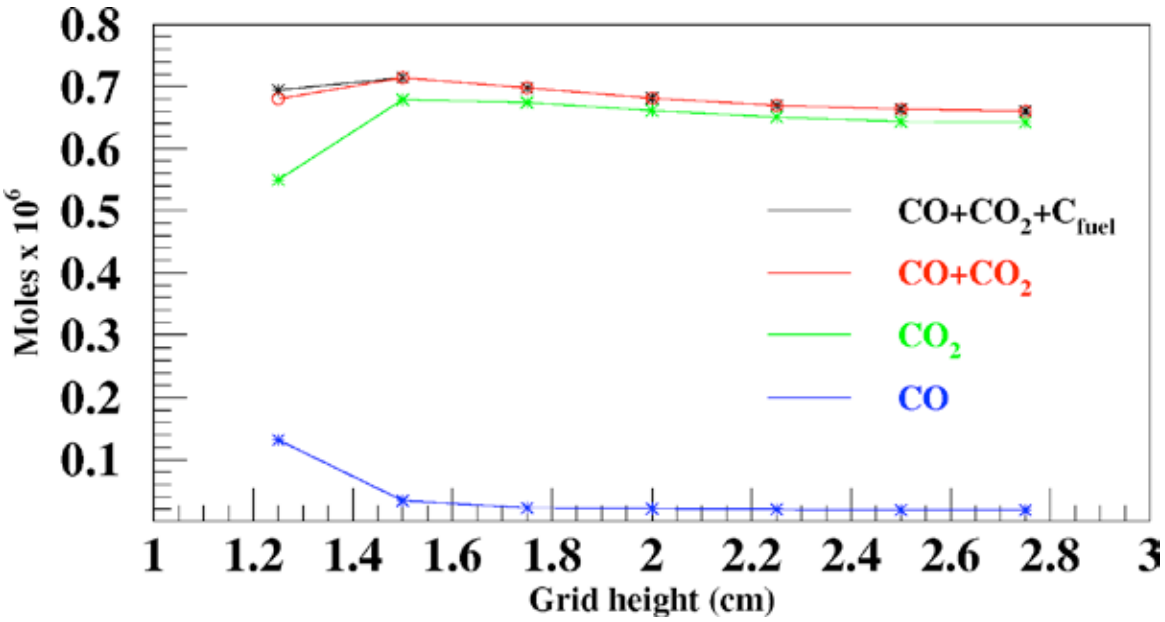

Figure 12: Moles of CO, CO_2, and total carbon (defined as CO+CO_2+fuel carbon).

Calculated within grid layers at the vertical coordinate Z = 1.25,1.5,1.75…up to Z = 2.75 cm by multiplying concentration (moles/cubic centimeter [cc]) by cell volume (cc) for each cell in the layer, and summing.

The blue CO curve drops by a factor of about 7 between Z = 1.25 and Z = 2.75 cm. This is far less than the ratio of maximum concentration in those same two planes, which are about 65,000 and 300 ppm, respectively. The green curve shows CO_2 formed between Z = 1.25 and 1.5 cm as CO is oxidized.

There is still a slight drop in all of the curves with increasing Z, likely caused by the exhaust gases undergoing buoyant acceleration and therefore increasing in Z-component of velocity with Z. To determine whether this is true, instead of summing concentrations through the cell layers, it is necessary to calculate and sum the species' flux (Figure 13).

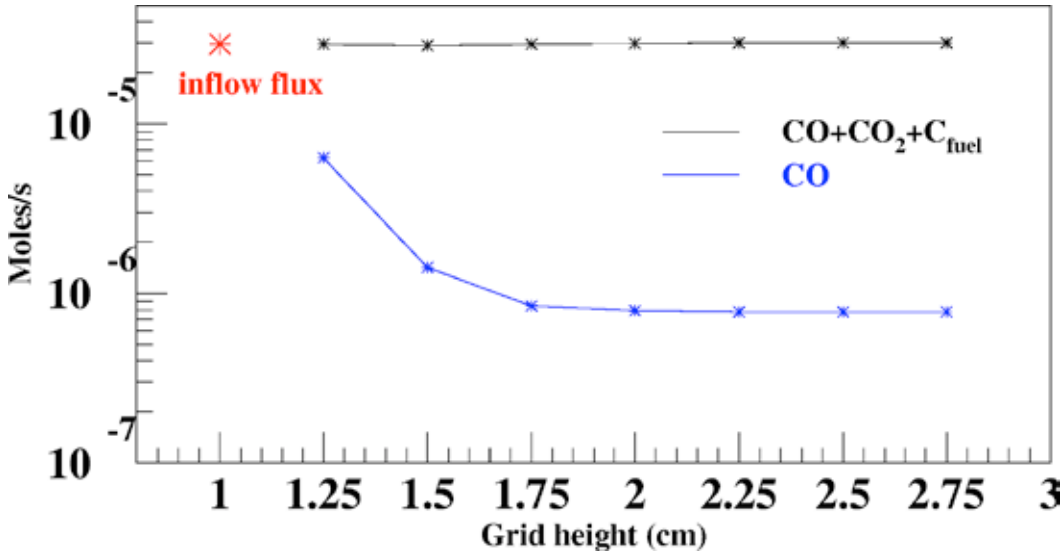

Figure 13: Flux of CO (blue) and total carbon (black) with increasing Z.

The single red point is the flux of carbon (CH_4,C_2H_6,C_3H_8) in the inflow duct. Flux is calculated by multiplying concentration (moles/cc) by cell volume (cc) by Vz (cm/s) for each cell in the layer, and summing.

The black $CO+CO_2+C_{fuel}$ curve is level, confirming the hypothesis. The single red data point added is the carbon atom flux from the three fuel species calculated in the inflow duct, and, except for any atmospheric CO_2 coming through the bottom and side boundaries, is the source of all carbon in the domain. Further, the agreement between the red point and the black line (and the overlap of black and red curves in Figure 12) indicates that using $CO+CO_2+C_{fuel}$ is sufficient to account for most of the carbon, at least in the post-flame region.

3.2.3. Nitrogen Oxides (NO_x)

As mentioned earlier in Section 2.4, our treatment of NOx uses only nitric oxide (NO) and omits NO_2, which is not included as a species in the C3+ Zeldovich chemical mechanism. While the relative ratios of NO and NO_2 are extremely important with regard to anthropogenic ozone production in the atmosphere, there are chemical equilibrium arguments that the NO_2 to NO production ratio is small above 1,500 K (Bowman 1991, Section 3.4).

Figure 14 shows the concentration profile of NO taken with lateral and head-on slices, as in the previous section. The high concentration areas are in the high-temperature region above the port, and they coincide with the region of high CO concentration and temperature.

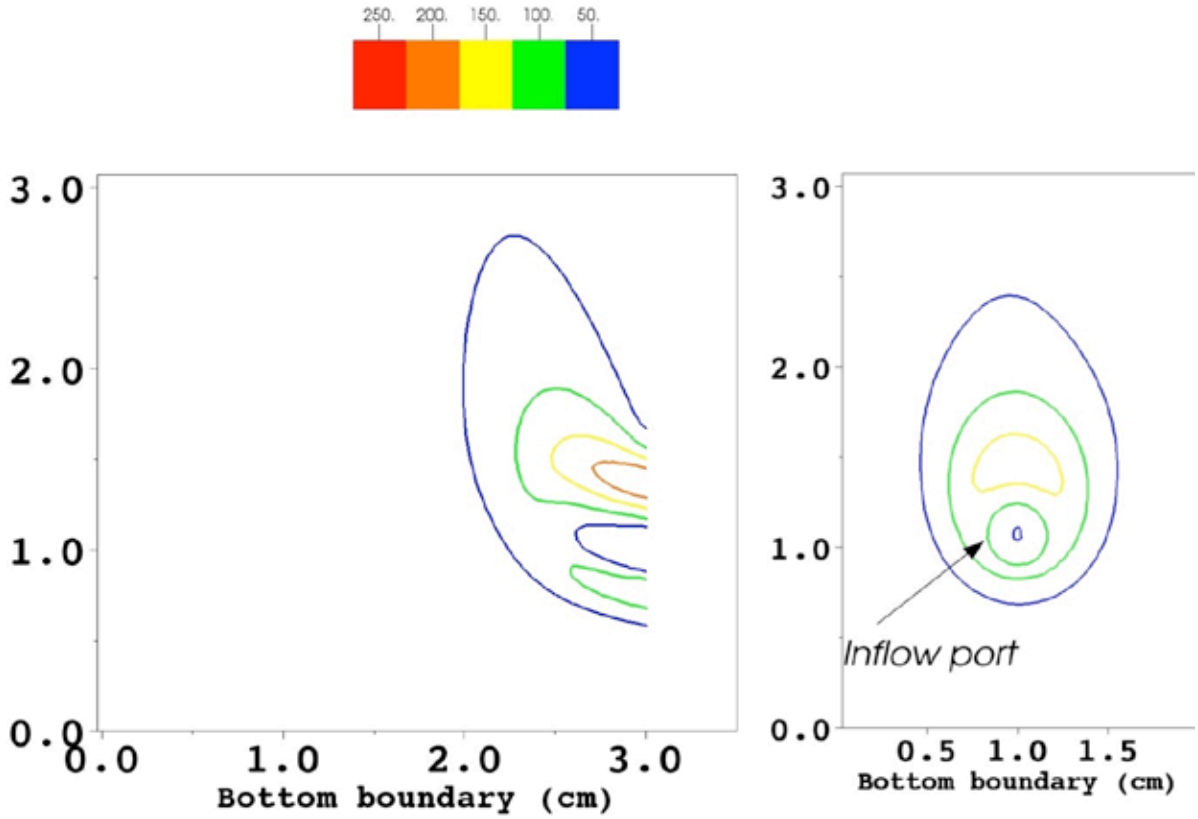

Figure 14: [NO] in ppm (mole fraction × 10^6).

Left panel: Sliced parallel to the inflow at central Y coordinate. Right panel: Sliced perpendicular to the inflow, at x = 2.6 cm; i.e., 0.4 cm from the port orifice, which is centered about (y,z) = (1.0,1.0).

As mentioned earlier in Section 2.4, NO is produced (Bowman 1991; Warnatz et al. 1995) solely by thermal Zeldovich reactions, as prompt NO chemistry is not well understood for propane (C3) and higher carbon number fuels. Since the peak temperature in this particular simulation is 2,144 K, (Figure 7) we expect thermal NO to account for most NO, and that the omission of prompt NO is not problematic. Additionally prompt NO production is expected to drop off significantly at the mixture stoichiometries of $\phi \approx 2.5$ that were used.

3.2.4. Formaldehyde

Figure 15 shows the concentration profile of formaldehyde for lateral and head-on slices. Formaldehyde is largely consumed within the flame and insignificant quantities exit the grid as a pollutant. This is consistent with laboratory Bunsen flame observations (Ashman and Haynes 1996) in which 120 ppm is sampled in the inner cone of the flame, most of which is consumed within the flame, and concentrations of about 20 ppm are observed near the flame base. The conclusions of that study are that formaldehyde as a pollutant results mainly from cooling of the flame by quenching near surfaces that conduct heat away, thereby suppressing reactions responsible for removing formaldehyde. Such quenching could occur on the lower surface of a cooking utensil, especially in the early stage of warming, when the contents are at room temperature or colder.

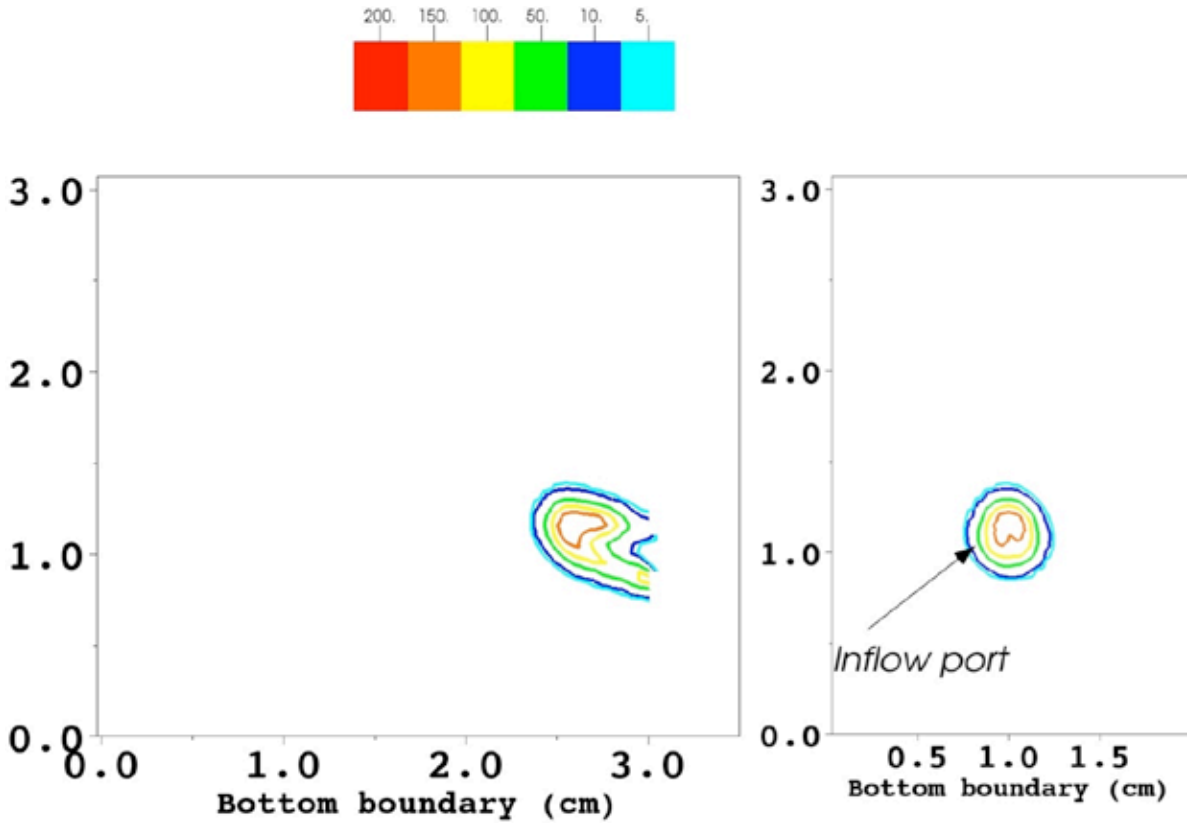

Figure 15: [Formaldehyde] in ppm (mole fraction × 10^6).

Left panel: Sliced parallel to the inflow at central Y coordinate. Right panel: Sliced perpendicular to the inflow, at x = 2.6 cm; i.e., 0.4 cm from the port orifice, which is centered about (y,z) = (1.0,1.0).

3.3. Dependence on Inflow Velocity and Equivalence Ratio

The dependence on the inflow velocity and equivalence ratio (ϕ) was examined with seven simulations using the baseline gas mixture (Table 1) and the five-point design (one full simulation per point) in Figure 2. Since two additional simulation points were available, (see Figure 2) that data has been included in the comparison. Plots in the remainder of this subsection are graphically arranged in the same manner as green asterisks and "+" signs from Figure 2.

3.3.1. Flame Appearance and Temperature Field

The flame appearance is shown in Figure 16. The trend with increasing inflow velocity (keeping ϕ constant) is for longer flame length and longer distance from the port to the point where burning commences, as well as farther flame extent in the horizontal direction. The trend with increasing ϕ (keeping velocity constant) is for a larger flame, since there is more fuel to burn. The flame front is farther from the port because the flame speed S_L decreases from $\phi = 2$ to $\phi = 3$, and for the higher ϕ, the flame must sit on an envelope where the inflow has diverged more and has a lower velocity than for the lower ϕ case. The unburned liftoff region is angled more sharply upward, possibly because of the increased combustion rate. These trends are in line with those predicted by the theory of diffusion flames (Gerstein 1991). The simulation with $v = 1.8243$ m/s and $\phi = 3$ has considerably higher energy delivery than the others, 38 MBtu/hr/in^2. It was conducted with a larger grid height out of concern that the domain would not be large enough. The horizontal extent of the flame is larger, as expected, but the flame height does not change as significantly as the horizontal extent. Table 2 shows the heat release and peak temperatures for this set of simulations.

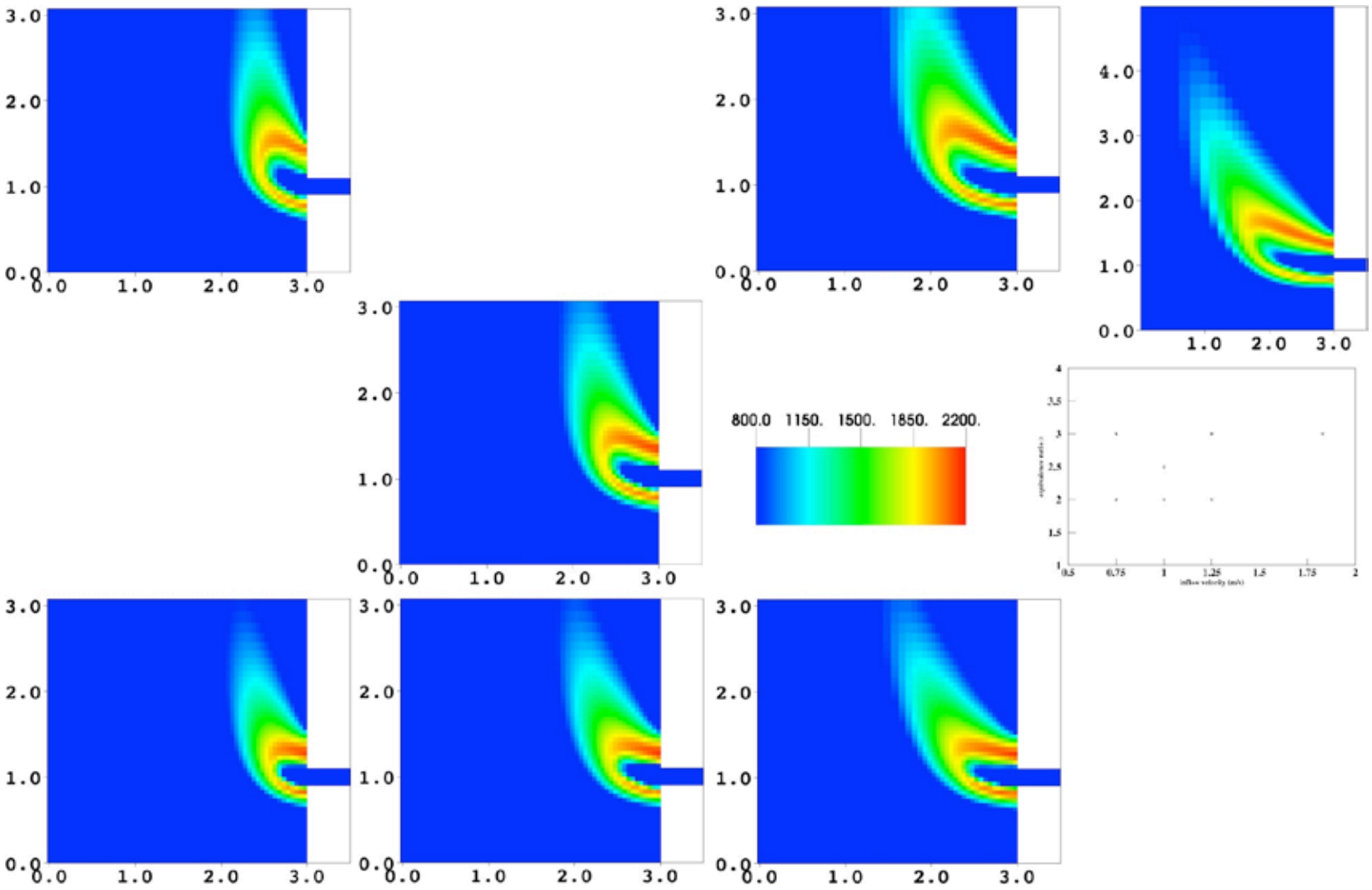

Figure 16: Flame appearance and temperature field in degrees K.

The second legend graphically shows the design layout (same as in Figure 2) of inflow velocity and ϕ.

Table 2: Flame and temperature properties as inflow velocity and ϕ are varied (baseline gas).

V=0.75m/s ϕ=3				**V=1.25m/s ϕ=3**		**V=1.8 ϕ=3**	
Peak T	2102 K			Peak T	2149 K	Peak T	2110 K
Heat release	2.727e-02 KJ/s			Heat release	4.646e-02 KJ/s	Heat release	6.95e-02 KJ/s
	9.298e+01 Btu/hour				1.584e+02 Btu/hour		2.369e+02 Btu/hour
	1.500e+04 Btu/hour/in^2				2.554e+04 Btu/hour/in^2		3.822e+04 Btu/hour/in^2
		V=1.00m/s ϕ=2.5					
		Peak T	2144 K				
		Heat release	3.123e-02 KJ/s				
			1.065e+02 Btu/hour				
			1.717e+04 Btu/hour/in^2				
V=0.75m/s ϕ=2		**V=1.00m/s ϕ=2**		**V=1.25m/s ϕ=2**			
Peak T	2133 K	Peak T	2155 K	Peak T	2151 K		
Heat release	1.945e-02 KJ/s	Heat release	2.611e-02 KJ/s	Heat release	3.326e-02 KJ/s		
	6.630e+01 Btu/hour		8.9e+01 Btu/hour		1.134e+02 Btu/hour		
	1.069e+04 Btu/hour/in^2		1.436e+04 Btu/hour/in^2		1.829e+04 Btu/hour/in^2		

3.3.2. Carbon Monoxide

Figure 17 shows the CO concentration contours in ppm, and Table 3 presents the associated concentration values. In all of the flames, the region of highest CO is just above the inlet port, (red contour), coinciding with the high temperature region from Figure 16. The sharp gradient decrease from 50,000 ppm contour to the 5,000 ppm indicates where much of the CO oxidation (to CO_2) occurs. Inlet port velocity appears to determine the contour shapes more than does stoichiometry; e.g., the v = 0.75 m/s cases (top and bottom left panels) show similar contour features, as do the v = 1.25 m/s cases. The trend is for increasing CO with both increasing inlet velocity and increasing ϕ. Moving from the left to right in the figure, CO appears to come increasingly from the high CO region immediately above the flame. This may be caused by flow features influenced by inflow velocity.

These calculations are for an open flame. It is possible that the introduction of a solid, thermally conducting upper boundary (to simulate a cooking utensil) would change the flow pattern. Increased thermal conduction could result in less CO being oxidized to CO_2.

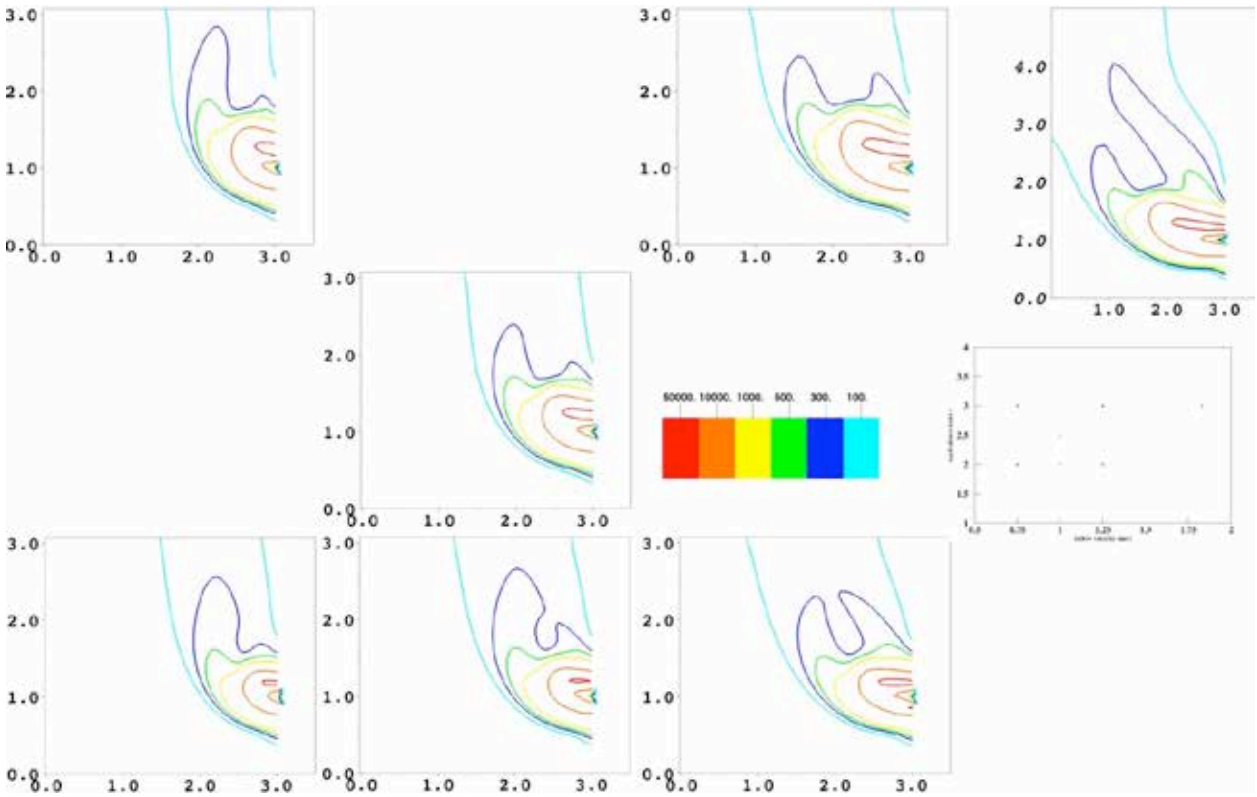

Figure 17: [CO] contours in ppm (mole fraction × 10^6) sliced parallel to the inflow.

Contours are unevenly spaced, selected to highlight both the sharp gradients within the flame, and the more gradual decrease post-flame. Middle right: Graphical legend depicting the velocity and ϕ of the inflows.

Table 3: Air-free concentrations calculated within the grid layer at vertical coordinate Z = 2.75 cm.

V=0.75m/s ϕ=3				**V=1.25m/s ϕ=3**		**V=1.82m/s ϕ=3**	
NO	150 ppm			NO	159 ppm	NO	137 ppm
CH_2O	3 ppb			CH_2O	1 ppb	CH_2O	14 ppb
CO	1509 ppm			CO	1341ppm	CO	1511 ppm
		V=1.00m/s ϕ=2.5					
		NO	146 ppm				
		CH_2O	0 ppb				
		CO	1368ppm				
V=0.75m/s ϕ=2		**V=1.00m/s ϕ=2**		**V=1.25m/s ϕ=2**			
NO	123 ppm	NO	133 ppm	NO	128 ppm		
CH_2O	0 ppb	CH_2O	1 ppb	CH_2O	1 ppb		
CO	1486 ppm	CO	1457 ppm	CO	1410 ppm		

Note: The concentrations were calculated by summing moles of pollutant, summing total gases with the exception of unused air, and recalculating concentration.

As discussed earlier in Section 3.2.2 the CO concentration drops not only because of its oxidation to CO_2 but also from the lateral spreading of the post-flame region and dilution of CO with air inflowing from the bottom of the grid. The effect of the dilution/mixing is removed in Figure 18 (in the same manner as in Figure 12) by summing the CO across horizontal slices (in the XY plane) taken across the entire grid at values of Z every 0.25 cm, starting at Z = 1.25 cm. Each slice is one cell layer thick. Note that the x-axis of Figure 18 is used to represent increasing values of Z (i.e., increasing height) of XY horizontal slices.

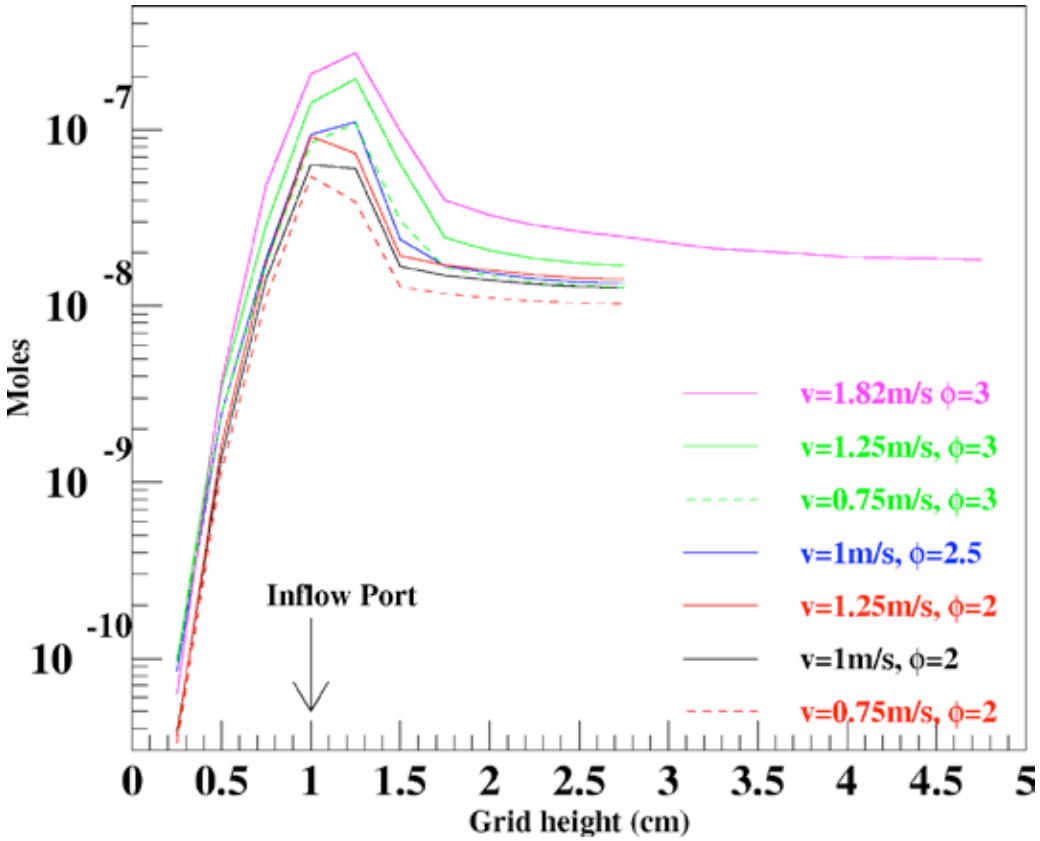

Figure 18: Moles of CO summed across XY planes at increasing height (Z in grid). Calculated by multiplying concentration (moles/cc) by cell volume (cc) for each cell in the layer and summing. The central design point is in blue.

The curves drop by factors between 4 and 10 in going from Z = 0.25 to Z = 2.75 cm.

3.3.3. Nitrogen Oxides (NO_x)

Nitrogen oxide concentration trends with inflow velocity and ϕ are shown as contour slices in Figure 19, and as summed molar concentrations in Figure 20.

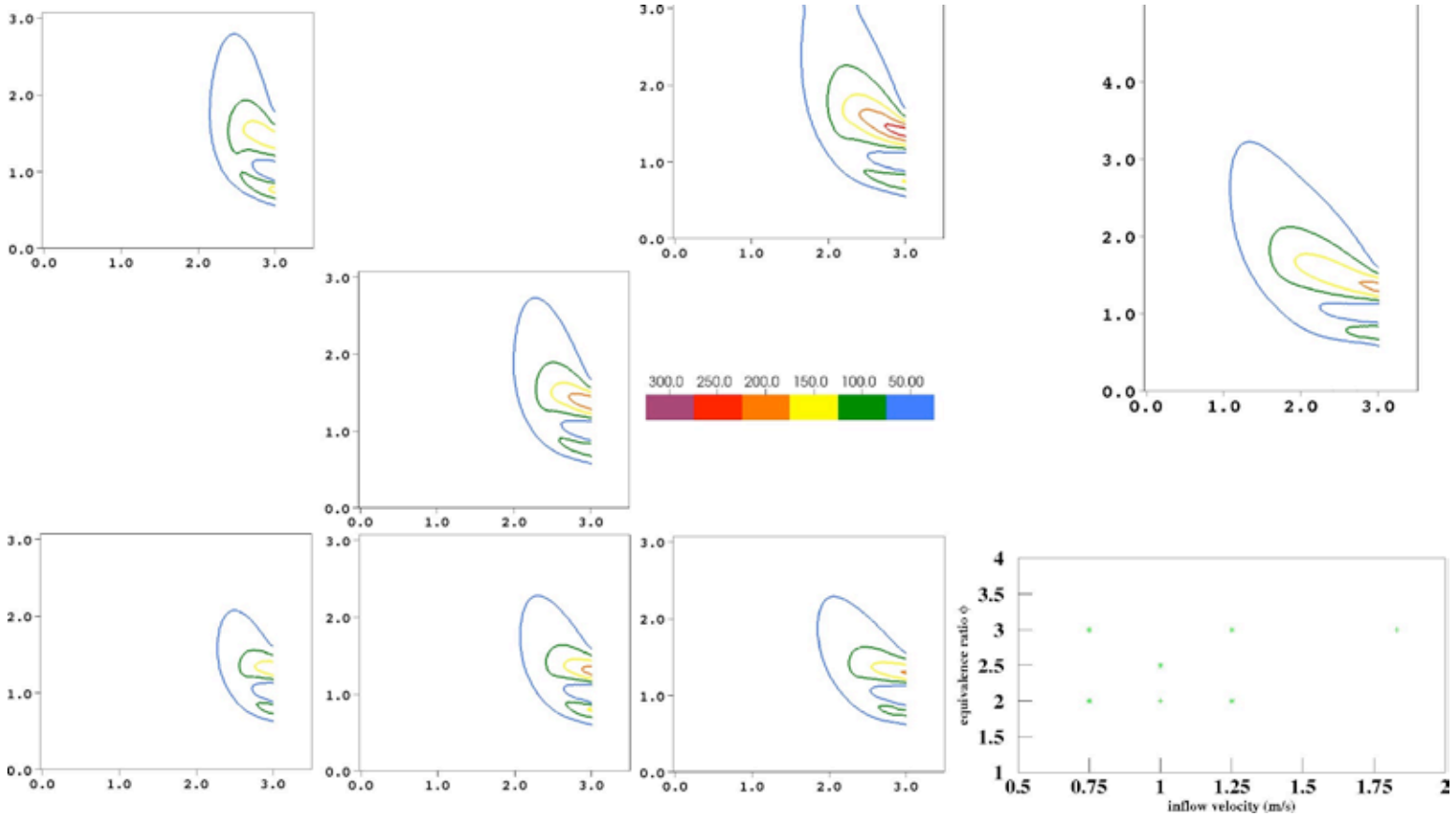

Figure 19: Thermal [NO] contours in ppm (mole fraction × 10^6) sliced parallel to the inflow.

Graphical legend depicts the velocity and ϕ of the inflows.

There is effectively no destruction of NO in the chemical mechanism used, as the reverse rates of these reactions are not dominant until the temperature is much higher. Therefore the drop in NO concentration with increasing Z occurs solely from the lateral spreading of the post-flame region and dilution with air inflowing from the bottom of the grid. This can be seen in Figure 20 where, as was done with CO, the effect of the dilution/mixing is removed by summing the NO across horizontal slices (in the XY plane) taken across the entire grid at chosen values of Z (every 0.25 cm starting at Z = 1.25 cm.). Each slice is one cell layer thick.

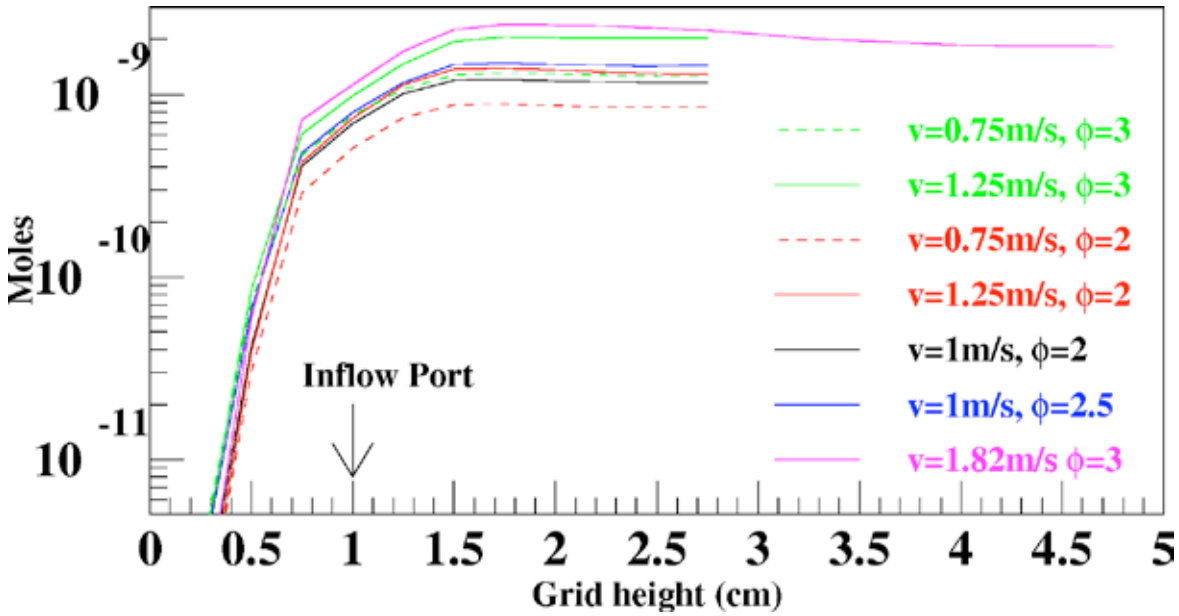

Figure 20: Moles of NO contained within grid layers at Z = 1.25,1.5,1.75 cm…up to Z = 2.75 cm. Calculated by multiplying concentration (moles/cc) by cell volume (cc) for each cell in the layer, and summing. The central design point is in blue.

The trend is for increasing NO with both increasing inlet velocity and increasing ϕ. The contours show that above and below the flame near the inlet are regions of higher concentration, particularly above. The NO below the port flows around the inlet jet to exhaust.

3.3.4. Formaldehyde

The formaldehyde created within the flame appears to be efficiently destroyed before it leaves the flame region, as discussed in Section 3.2.4. This occurred for all the simulations and is not discussed further.

3.4. Comparison of the Baseline Gas, Gas 3A, and Gas 3C

Comparison between the various gases (described in Section 2.2.1, Table 1) uses the central design point (v = 1 m/s, ϕ = 2.5) for the baseline gas. For Gases 3A and 3C the same volumetric ratio of fuel to primary air was used, in effect as if the gas composition in the supply line had been changed. Other than the change in inflowing gas composition, there are no differences between simulations. In going from baseline to 3A to 3C, ethane rises monotonically, while propane is highest for 3A, then 3C, and lowest in the baseline fuel. The heating values for 3A

and 3C are approximately equal, while the baseline fuel is about 7% lower. The Wobbe number for the baseline fuel is 5.7% lower than for the other two gases.

3.4.1. Flame Appearance and Temperature Field

The temperature fields are very similar in shape, features, and maximum temperature (Figure 21).

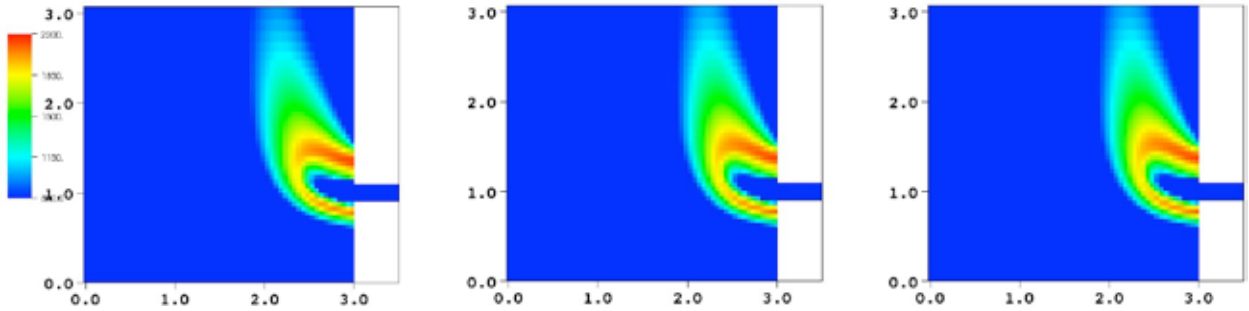

Figure 21: Temperature fields comparing gases baseline, 3A, and 3C.

3.4.2. Carbon Monoxide

The CO spatial fields (Figure 22) and the air-free CO concentration in

Table 4 are also very similar in appearance. The high CO region immediately above the port is slightly larger for Gases 3A and 3C, likely because of their higher heating values.

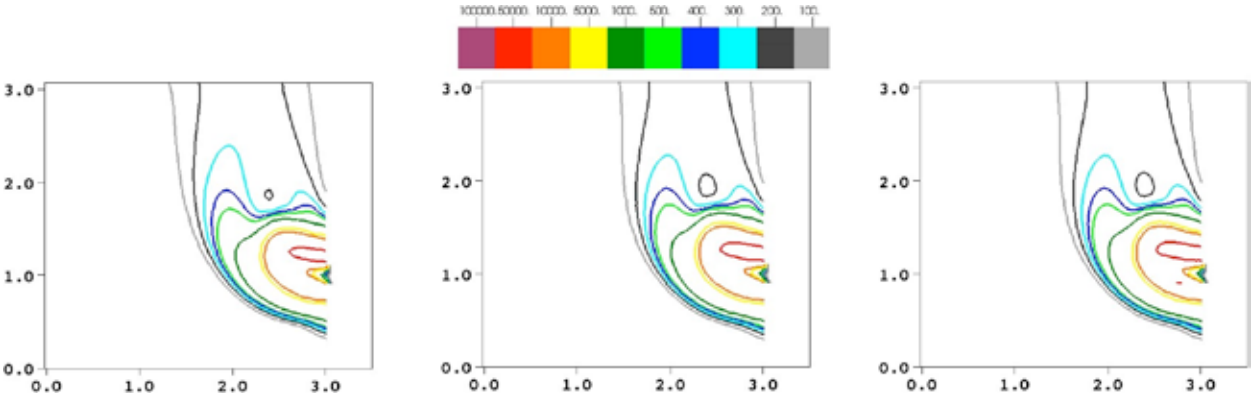

Figure 22: CO contours comparing gases baseline, 3A, and 3C.

Table 4: Air-free concentrations calculated within the grid layer at vertical coordinate Z = 2.75 cm.

	Baseline	Gas 3A	Gas 3C
NO (ppm)	146	156	156
CH_2O (ppb)	0	0	0
CO (ppm)	1368	1327	1325

Note: The concentrations were calculated by summing moles of pollutant, summing total gases with the exception of unused air, and recalculating the concentration. All cases use v = 1 m/s and ϕ = 2.5. Note that the CH_2O concentrations are in parts per billion (ppb).

Summing CO across layers results in slightly higher CO (Figure 23) for Gases 3A and 3C, but the difference is surprisingly small.

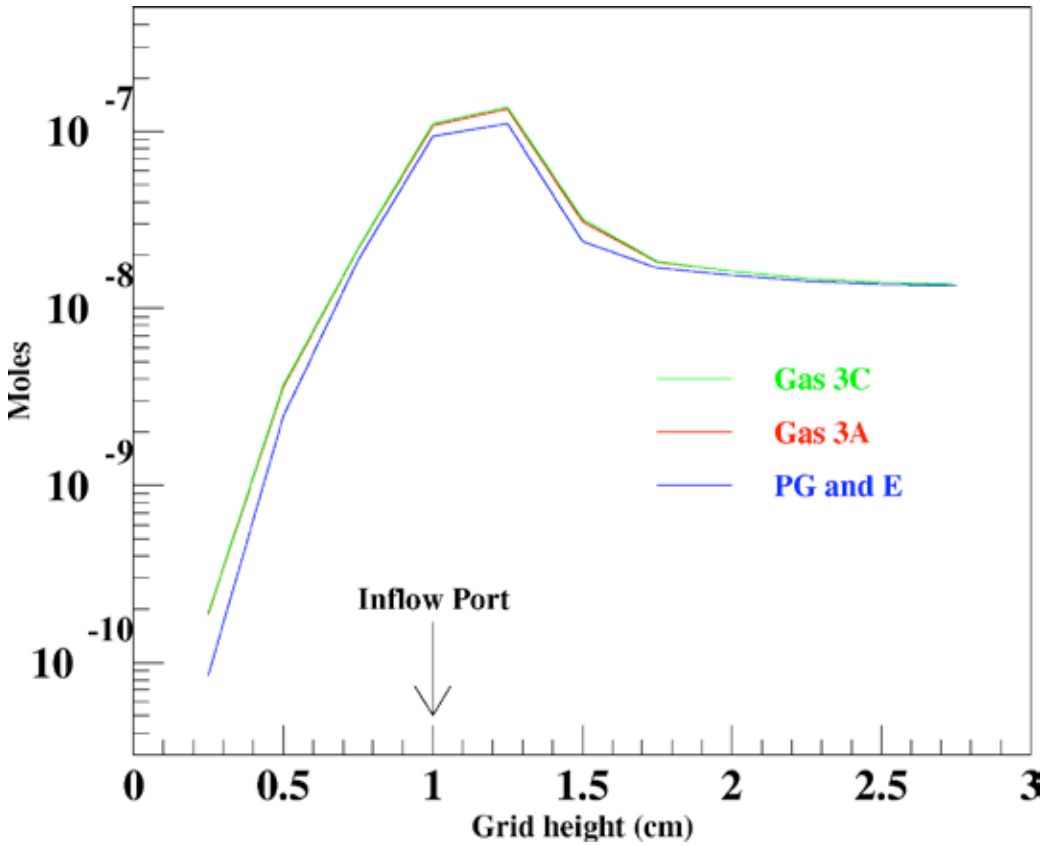

Figure 23: Moles of CO across grid layers of varying height; comparison of baseline and simulated LNG blends (3A, 3C).

Carbon monoxide is the penultimate oxidation product of the three fuel hydrocarbons. By comparing some earlier intermediate species and radicals it can be determined why overall CO production from the three fuels is similar. Figure 24 and Figure 25 both show chemical species concentrations along a streamline in the same manner as those shown in Figure 8 and Figure 9. These species are those of the oxidation sequence of ethane and propane, which are linked, as

they have common intermediates. A simplified picture of this (repeated from Section 2.4.) in the C3 mechanism reminds us that:

- Ethane initially goes primarily to C_2H_5, which then goes to C_2H_4 and so on.
- Propane proceeds through repeated abstraction of H from the propane molecule:

$$C_3H_8 \rightarrow C_3H_7 \rightarrow branching\ mainly\ to\ \frac{C_3H_6 \rightarrow C_2H_4}{C_2H_5 \rightarrow C_2H_6\ or\ C_2H_4}$$

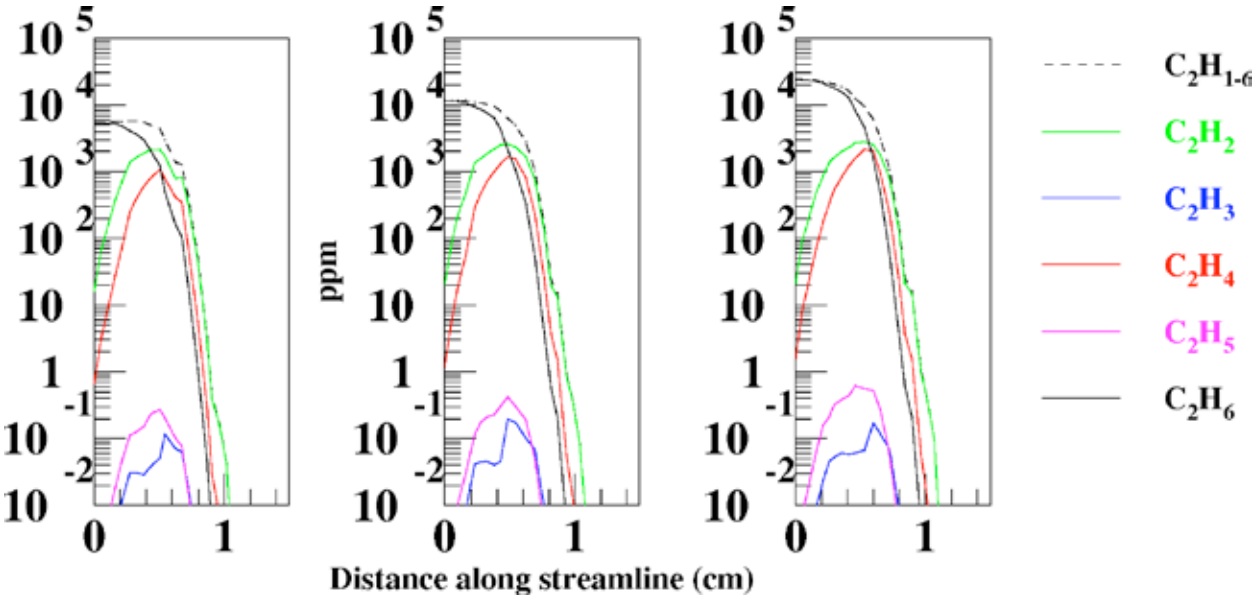

Figure 24: Comparison of C_2 intermediates along a streamline for gases baseline, 3A, and 3C.

The intermediates ethylene (C_2H_4) and acetylene (C_2H_2) occur in high concentrations in Figure 24, for all three of the gas mixtures. Note that small concentrations, such as C_2H_5, are not necessarily unimportant. The concentrations are small because the associated lifetimes of the species are short; if viewed in a reaction flux diagram[3] they would be seen to be playing a significant role. The changes in intermediates such as ethylene and acetylene are less marked than the changes in the C_2H_6 fuel itself. This is confirmed in Table 5, where ratios of intermediates to fuel are shown. Intermediates closer in the oxidation sequence to the fuel show more similarity between the three gas mixtures (baseline, 3A, and 3C) than intermediates farther down. For example, the C_2H_5/ethane ratios differ by a factor of two, while the C_2H_2/ethane ratios differ by a factor of four. Intermediates farther down in the sequence have more of a mixed contribution from the three fuels (methane, ethane, and propane), whereas those immediately adjacent to a fuel are more likely to have arisen from that fuel. Qualitatively, this is why carbon monoxide production is so similar between the three gas mixtures.

[3] Reaction flux diagrams trace the flow paths, and the rates of flow, of atoms/molecules starting from fuel, through multiple intermediate species, to final products.

Table 5: Peak ethane along streamline and ratios of peak C_2 intermediates to peak ethane.

Gas	Ethane (ppm)	C_2H_5/ethane	C_2H_4/ethane	C_2H_3/ethane	C_2H_2/ethane
Baseline	5.47e+03	5.0E-05	0.20	2.1E-05	0.39
3A	1.16E+04	3.6E-05	0.14	1.7E-05	0.22
3C	2.40E-04	2.6E-05	0.09	7.0E-06	0.11

Figure 25 and Table 6 show the same information as Figure 24 and Table 5, but for the C3 intermediates and the oxidation sequence of propane. They show similar behavior.

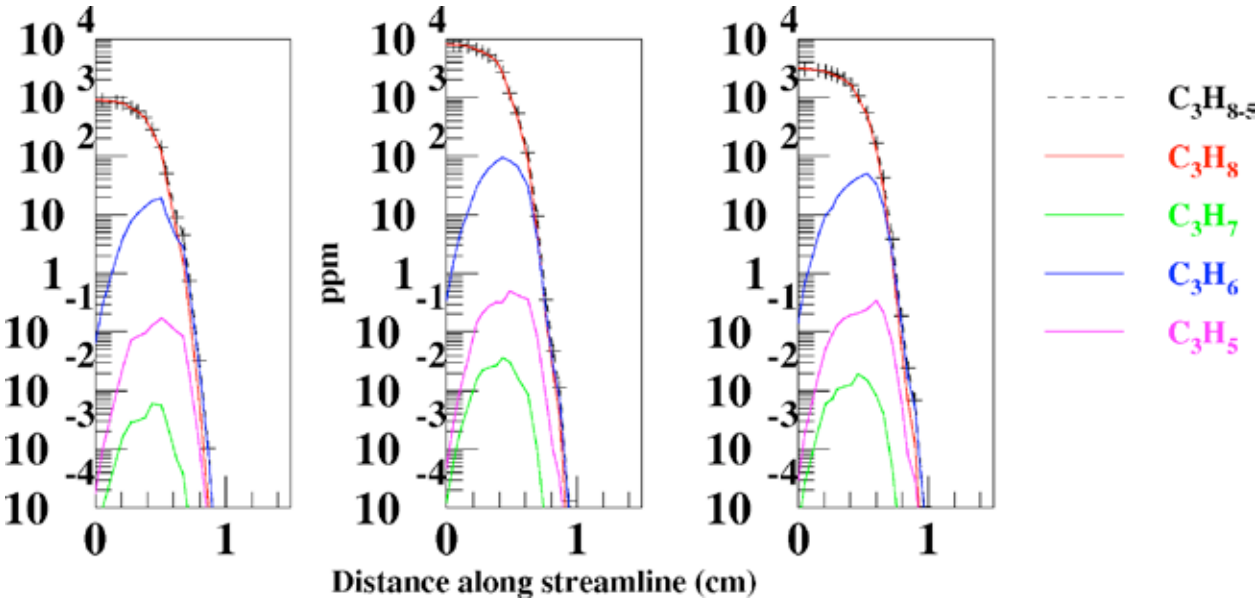

Figure 25: Comparison of C_3 intermediates along a streamline for (left to right) baseline, 3A, and 3C.

Table 6: Peak propane along streamline and ratios of peak C_3 intermediates to peak propane.

Gas	Propane (ppm)	C_3H_7/propane	C_3H_6/propane	C_3H_5/propane
Baseline	912	6.6E-06	2.0E-02	1.8E-04
3A	8080	4.5E-06	1.2E-02	6.2E-05
3C	3140	6.1E-06	1.6E-02	1.1E-04

3.4.3. Nitrogen Oxides (NOx)

The NO_x contours (not shown) were also very similar. Figure 26 below shows the molar sum of NO for the three gases, with an increasing Z coordinate.

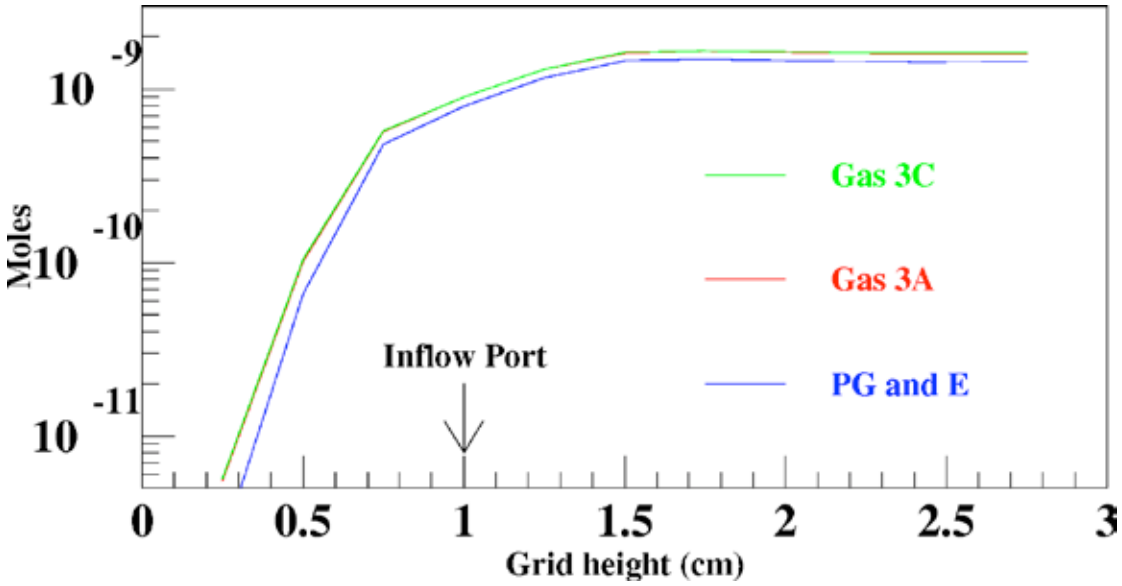

Figure 26: Moles of NO across grid layers of varying height; comparison of baseline and simulated LNG blends (3A and 3C).

3.4.4. Formaldehyde

Formaldehyde showed no significant variation between gases.

3.5. Comparison of 0.1 cm and 0.5 cm Port Lengths

Chronologically after completion of many of the simulations it was realized that a 0.5 cm port length was larger than in most residential range-top burners. The port length should correspond to the thickness of metal used in the outer rim of the disk from which the mixture of gas and air issues, and is typically no more than 0.1–0.2 cm, and not 0.5 cm as initially assumed. This difference may have consequences on the profile of the velocity entering the main grid from the port because of viscous drag between the gas and the port wall. At the inflow end of the port the velocity profile of the inflowing gas is flat (i.e., uniform). As the gas flows through the port it acquires a Poiseuille flow (parabolic) velocity profile, caused by viscosity reducing the tangential component of velocity at the wall. The longer the port, the more time the flow profile has to become parabolic.

Would a shorter port make a significantly different outcome of flame appearance, CO, and such? To address this concern a simulation was conducted at the central design point and baseline gas, with a 0.1 cm port length instead of 0.5 cm, but identical in all other respects. Inflow velocity at the right side of the port is a flat profile with magnitude 1 m/s in both runs. Figure 27 compares the velocity profiles across the port near junction of the port and main grid. In both cases drag reduces velocity at the wall and some of that flow is shifted toward the center, so that in both cases central velocity is greater than the incident 1 m/s. As expected, the short port simulation has had less time to reduce the velocities at the edges, and therefore has a lower peak value.

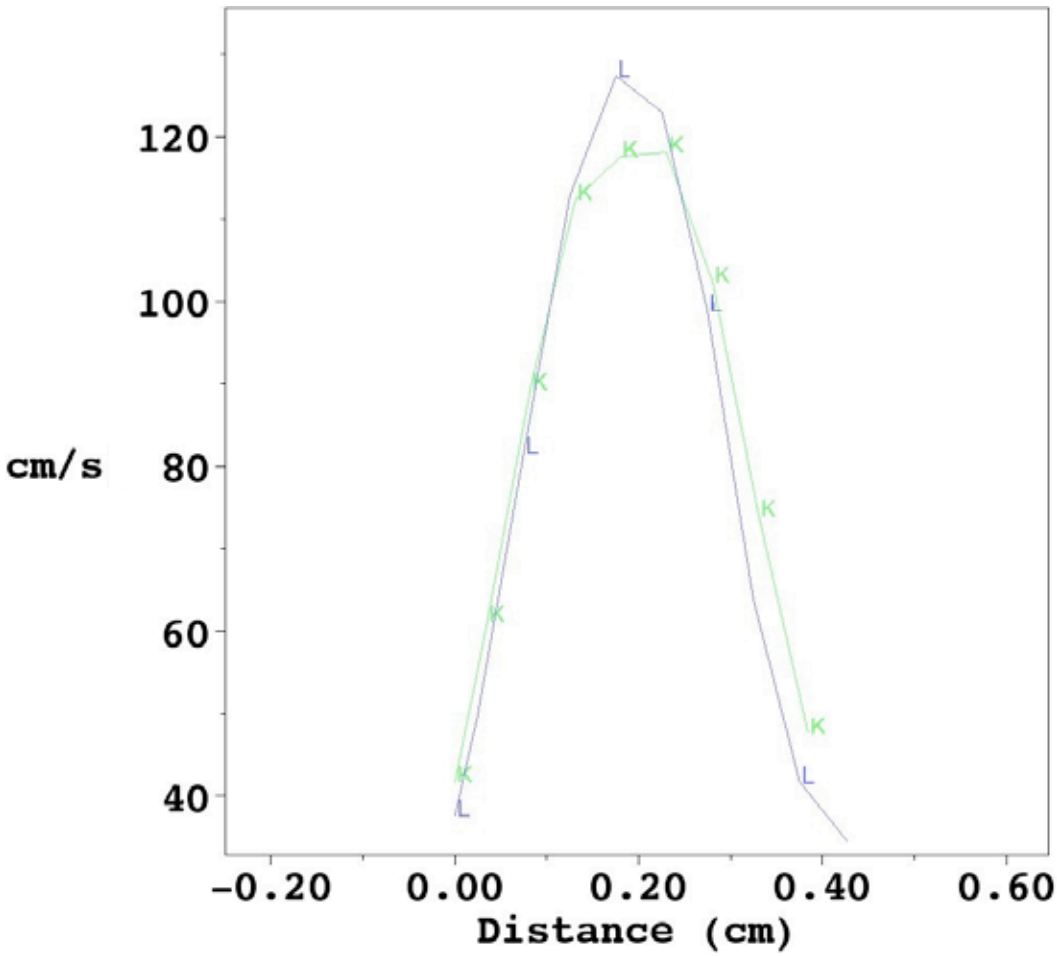

Figure 27: Velocity profiles with a 0.5 cm port (L points) and a 0.1 cm port (K points).

The profiles are taken along a line perpendicular to the flow across the port, just inside the main grid near the port exit. The port is centered at approximately 0.2 cm in this figure.

The overall velocity field reflects this difference (Figure 28) but the difference decreases with distance from the port.

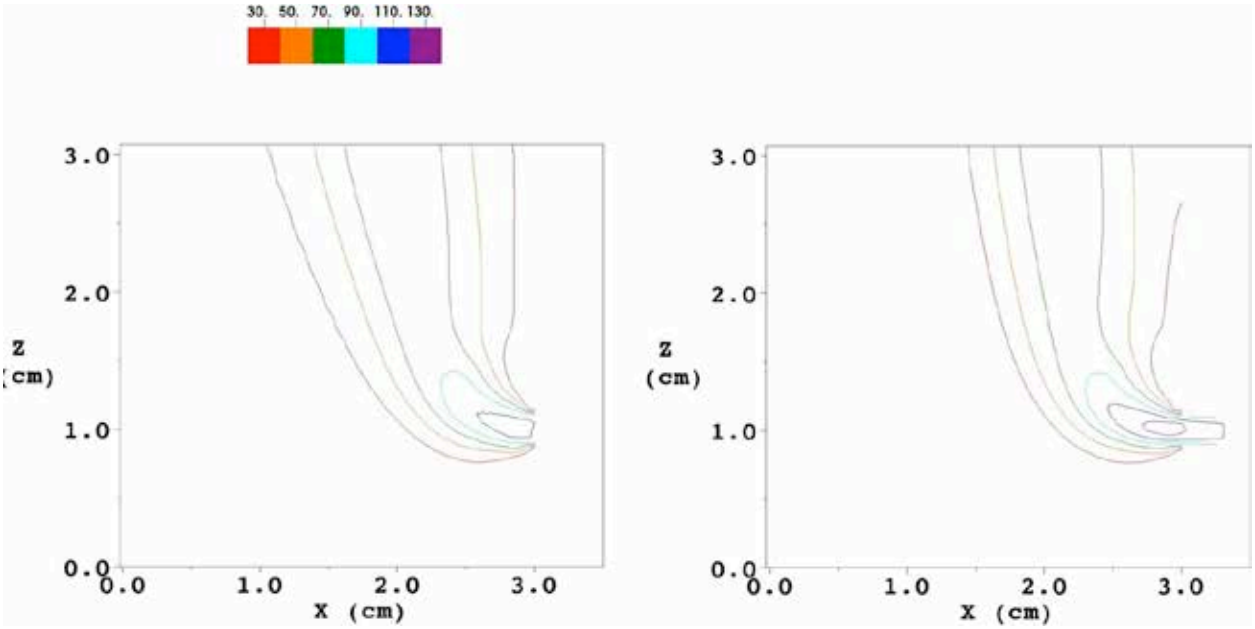

Figure 28: Contours of velocity magnitude. Left panel: 0.1 cm port. Right panel: 0.5 cm port.

The temperature fields (Figure 29) show peak temperature rising from 2,144K to 2,153K. Lateral flame extent is slightly more in the 0.1 cm port case.

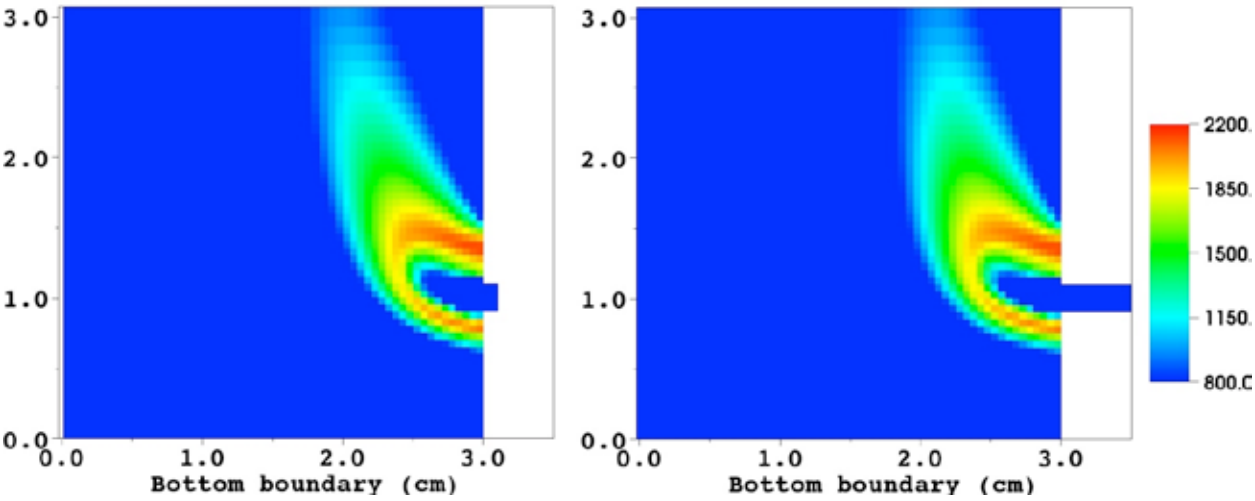

Figure 29: Temperature fields. Left panel: 0.1 cm port. Right panel: 0.5 cm port.

Differences are more apparent in the CO spatial field contour plots (Figure 30). The trend in this difference is similar to that seen in the sensitivity analysis of Section 3.3. The behavior of the CO fields can be seen in Figure 17, where the lower fork of the 300 ppm CO contour extends farther for the lower inflow velocity cases. Additionally, in going from a 0.5 cm to a 0.1 cm port, the peak CO has risen from 64,570 ppm to 66,160 ppm. The higher-concentration CO contours do not appear to have changed substantially.

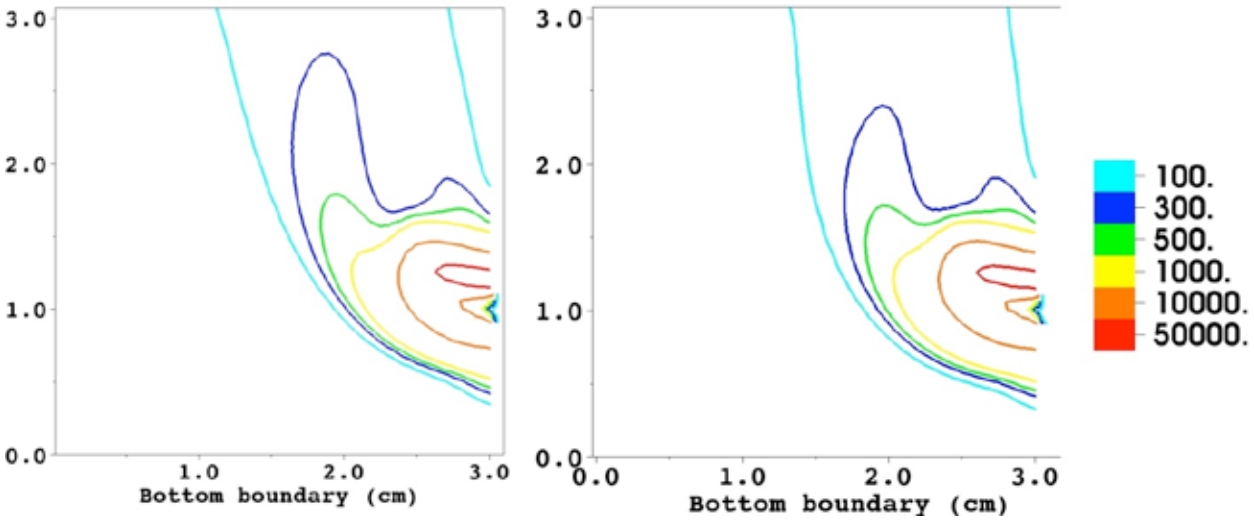

Figure 30: CO contours. Left: 0.1 cm port. Right: 0.5 cm port.

A similar port length comparison was made for the high heat-release case (v = 1.8 m/s, ϕ = 3, baseline gas). The difference in spatial CO for this condition is more marked (Figure 31), with the right fork of the 300 ppm contour extending about 1 cm less than before. The air-free CO concentrations at height Z = 2.75 cm are 1,452 ppm and 1,510 ppm for the 0.1 cm and 0.5 cm port cases, respectively.

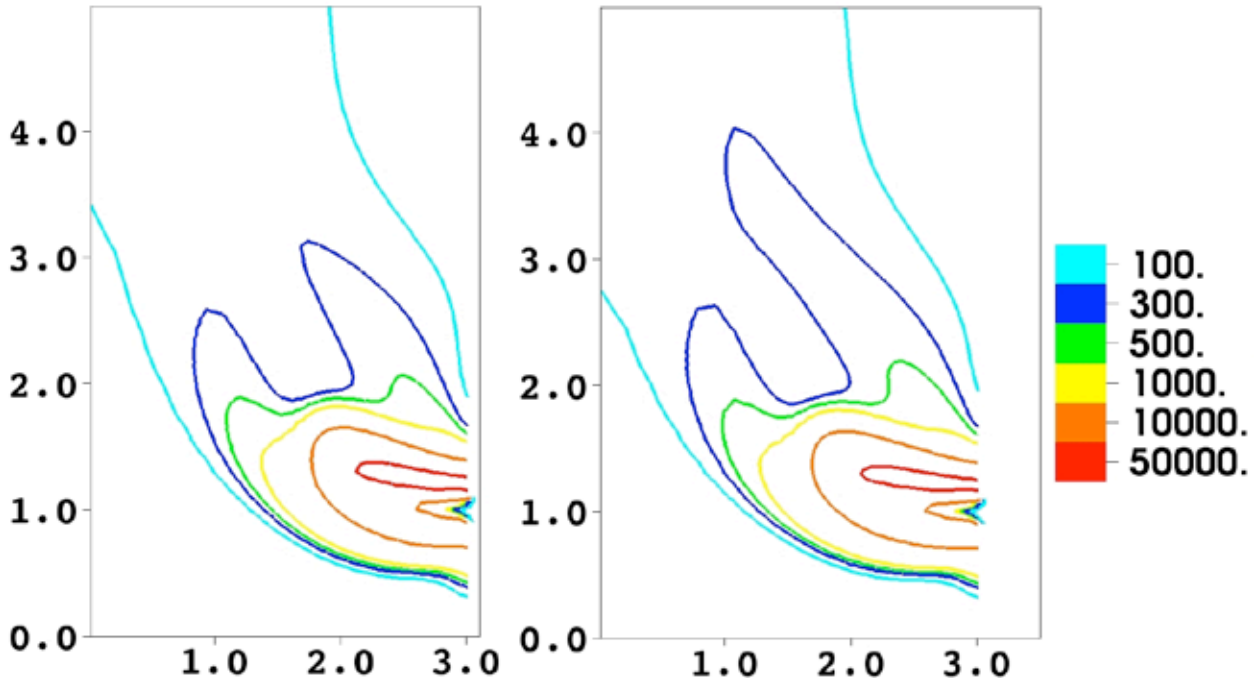

Figure 31: CO contours, high heat-release case. Left: 0.1 cm port. Right: 0.5 cm port.

In summary, for the central design point comparison the change in port length makes very little difference in terms of temperature fields and CO within the main grid. We believe the broader results and trends from earlier runs are applicable to the shorter port. For the high heat-release case, the difference is more apparent, especially in the CO field topology. Air-free CO concentrations are 3%–4% lower with a 0.1 cm port length.

3.6. Gas-Mixture Comparison of Higher Heat-Release Cases

A final set of simulations was conducted to compare the three gas mixtures for the high heat-release case (v = 1.8 m/s, ϕ = 3). The port length used is 0.1 cm. This set is useful for (1) comparison between the gas mixtures, and (2) comparison to the lower heat-release cases of Section 3.4, where gases were compared at the central design point. As was the case in Section 3.4, the specified stoichiometry was applied only to the baseline gas while gases 3A and 3C used the resulting volumetric ratio of fuel to primary air, in effect as if the gas composition in the supply line had been substituted with no other changes.

3.6.1. Flame Appearance and Temperature Field

The temperature fields (Figure 32) are very similar in shape, features, and maximum temperature. A small difference in flame heights can be seen in the case of the baseline gas (left panel). Likely this is a result of its lower heating value.

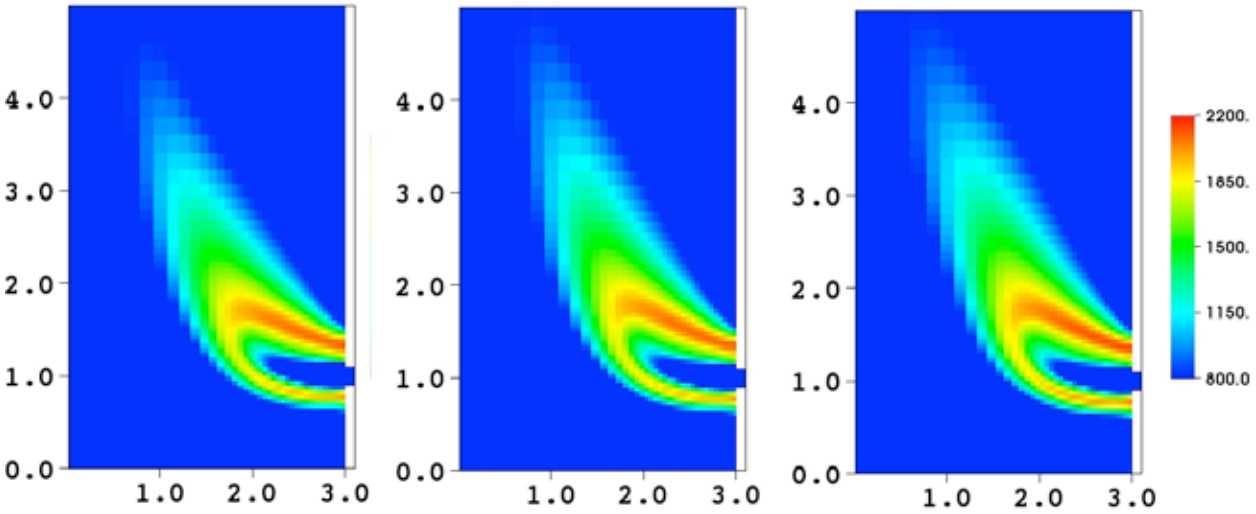

Figure 32: Temperature fields comparing gases baseline, 3A, and 3C.

3.6.2. Carbon Monoxide

Between the three cases, the CO spatial fields (Figure 33) are similar in appearance. As in Figure 22, the high CO region immediately above the port is slightly larger for Gases 3A and 3C, likely because of their higher heating values.

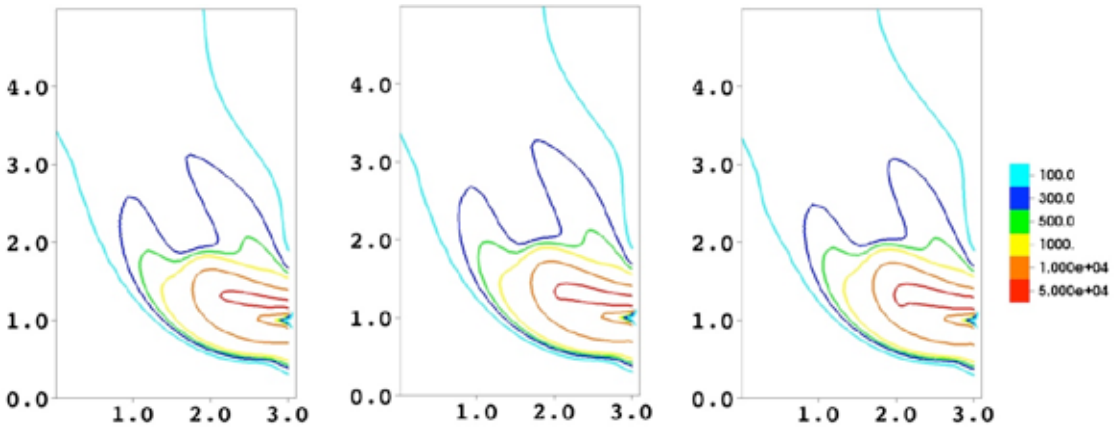

Figure 33: CO contours comparing gases baseline, 3A, and 3C.

Summing CO across layers (

Figure 34) results in a total CO about a factor of two higher than the total CO in Figure 23. The overall shape of the curves and the differences between gases is not very different. Table 7 shows the air-free CO concentration for this condition; results are similar to those presented in

Table 4.

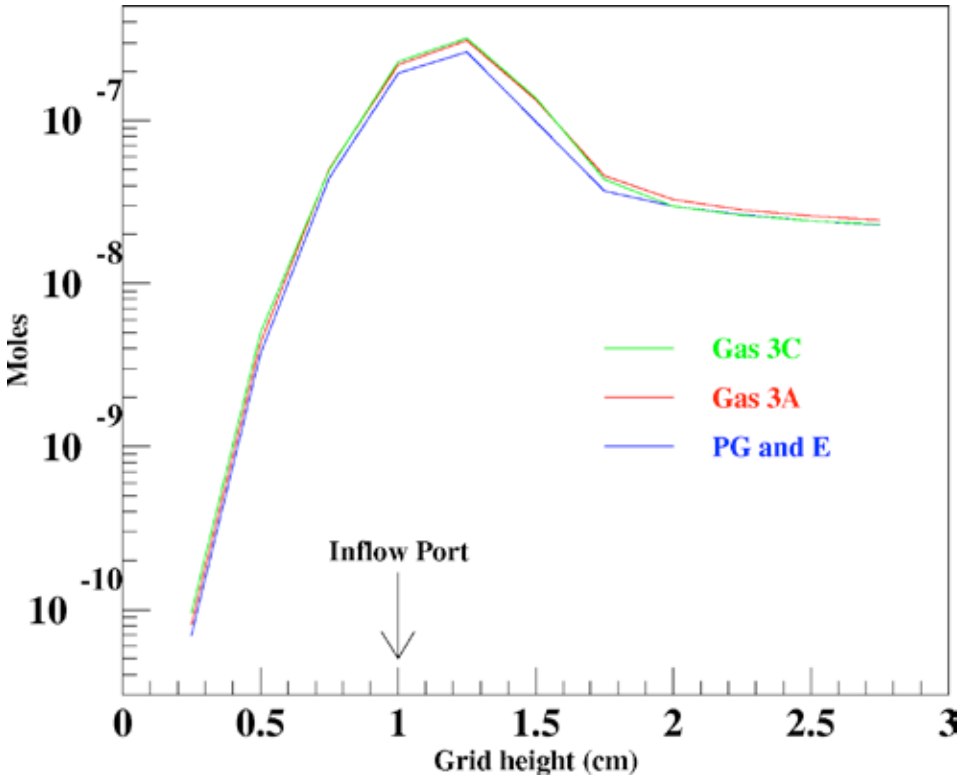

Figure 34: Moles of CO across grid layers of varying height; comparing baseline and simulated LNG gases 3A and 3C.

Table 7: Air-free concentrations calculated within the grid layer at vertical coordinate Z = 2.75 cm.[1]

	Baseline	Gas 3A	Gas 3C
NO (ppm)	141	151	164
CH_2O (ppb)	8	8	2
CO (ppm)	1452	1444	1328

[1] Calculated by summing moles of pollutant, summing total gases with the exception of unused air, and recalculating the concentration. All cases use v = 1.8 m/s and $\phi = 3$. Note that the CH_2O concentrations are in ppb.

Following the same method of Section 3.4.2 of following chemical species concentrations along streamlines,

Figure 35 and

Figure 36 show concentrations of C_2H_6 and selected C_2 intermediates along the central streamline.

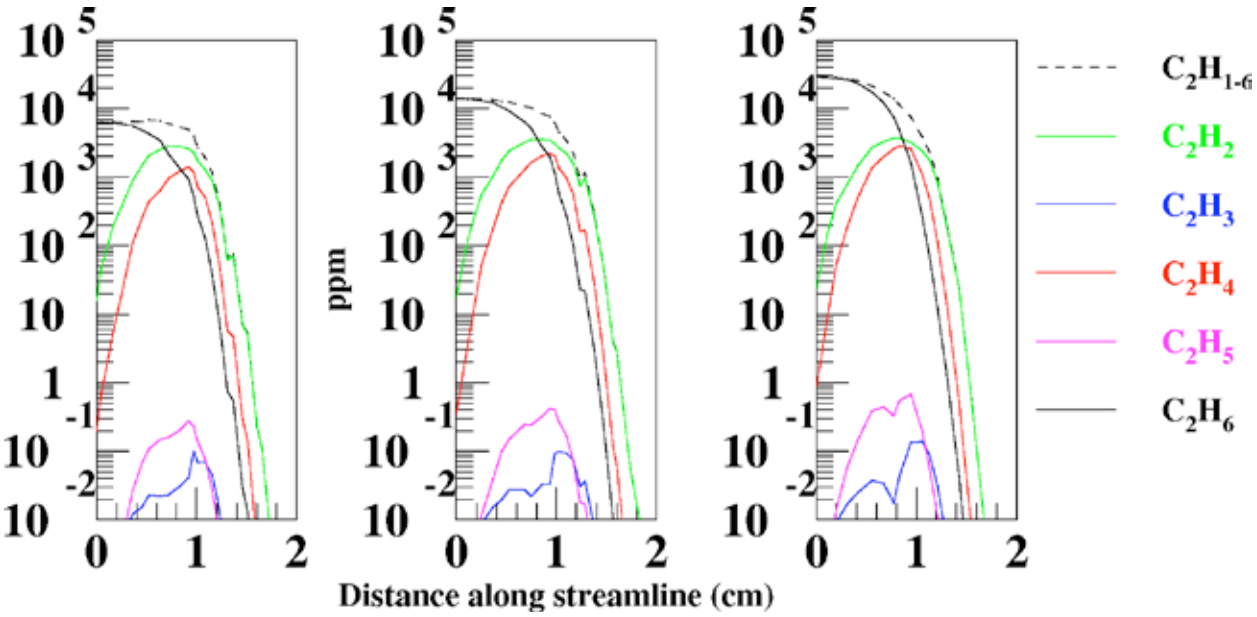

Figure 35: Comparison of C_2 intermediates along a streamline for gases baseline, 3A, and 3C.

No changes of significance were observed, although, as expected, the extent was increased, due to the higher inflow velocity.

Table 8: Peak ethane along streamline and ratios of peak C_2 intermediates to peak ethane.

Gas	Ethane (ppm)	C_2H_5/ethane	C_2H_4/ethane	C_2H_3/ethane	C_2H_2/ethane
Baseline	6.27e+03	4.4e-05	0.22	1.6e-05	0.46
3A	1.38e+04	3.0e-05	0.16	7.0e-06	0.26
3C	2.87e+04	2.4e-05	0.10	4.7e-06	0.13

In

Figure 36 and Table 9, C_3H_8 and selected C_3 intermediates are tracked along the central streamline. Again, no significant deviations from Figure 25 and Table 6 are seen.

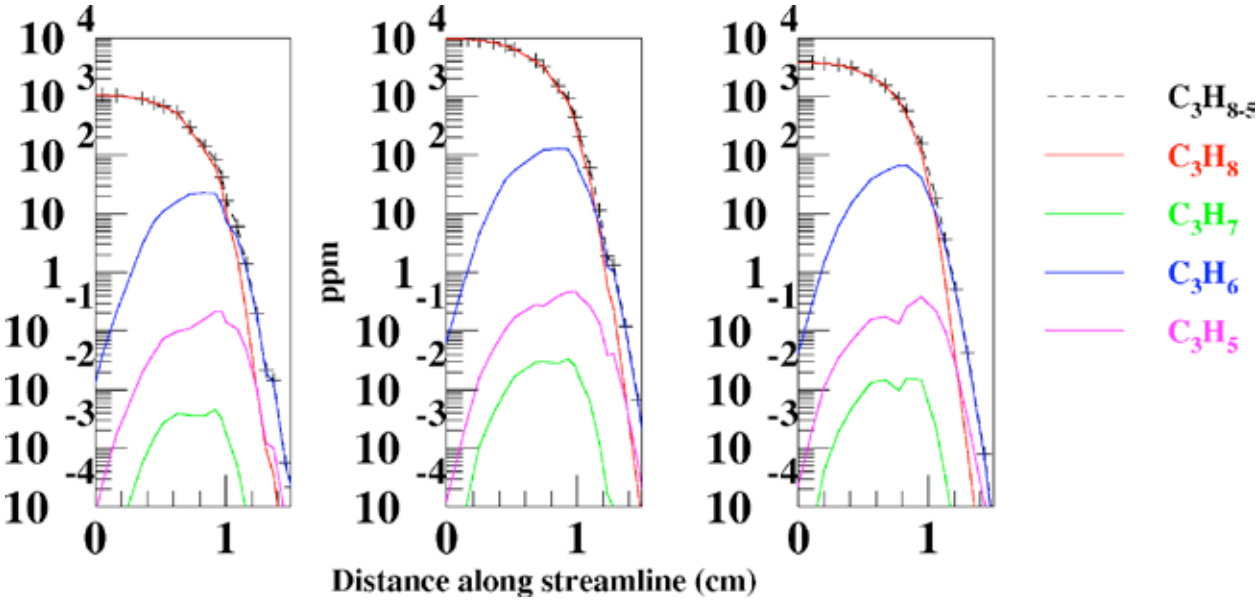

Figure 36: Comparison of C_3 intermediates along a streamline for (left to right) gases baseline, 3A, and 3C.

Table 9: Peak propane along streamline and ratios of peak intermediates to peak propane.

Gas	Propane (ppm)	C_3H_7/propane	C_3H_6/propane	C_3H_5/propane
Baseline	1040	4.4E-06	2.0E-02	2.1E-04
3A	9660	3.4E-06	1.3E-02	4.9E-05
3C	3760	4.1E-06	1.8E-02	1.0E-04

3.6.3. Nitrogen Oxides (NOx)

Figure 37 shows the molar sum of NO for the three gases, with increasing Z coordinate. The difference between gases is slightly more apparent than was the case in Section 3.4.3; however, the slight drop in NO above heights of 2.5 cm is caused by NO leaving through the lateral front and back boundaries, as the overall flame is slightly larger for this higher heat-release case.

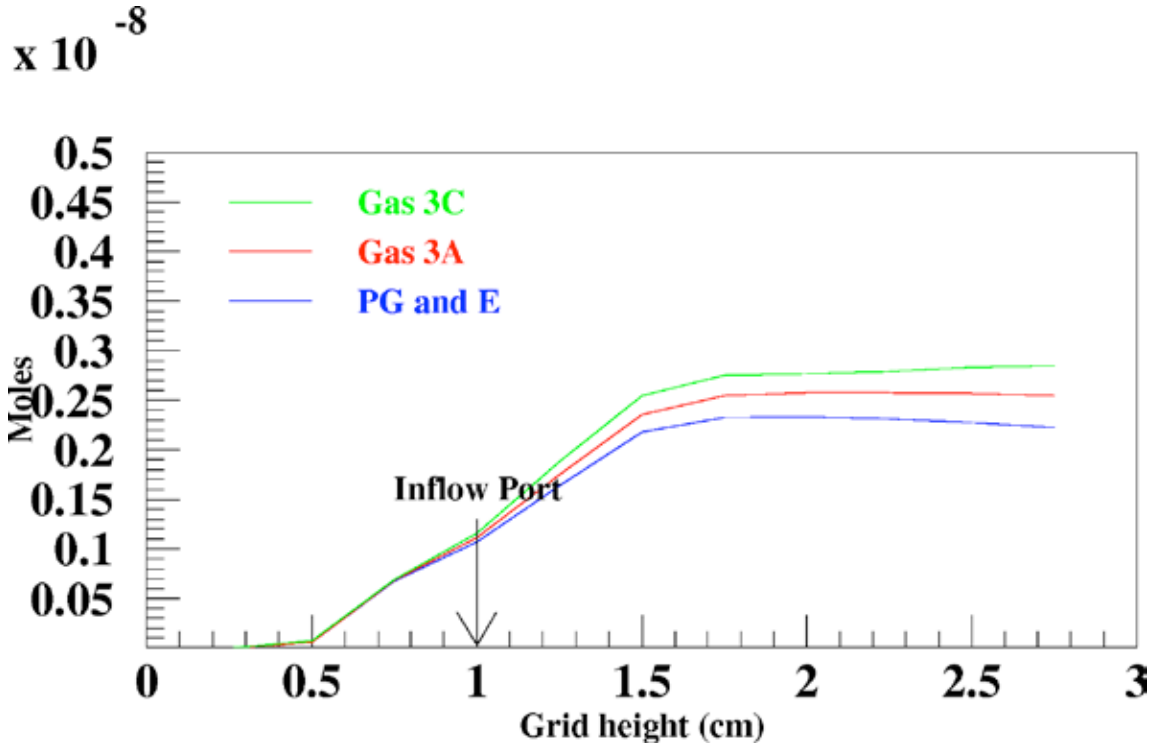

Figure 37: Moles of NO across grid layers of varying height; comparing baseline and simulated LNG gases 3A and 3C.

3.6.4. Formaldehyde

Formaldehyde showed no significant variation between gases, as can be seen in Table 7.

4.0 Conclusions

4.1. Overview and Context

We conducted numerical CFD-based three-dimensional computer modeling of a laminar flame to simulate a single port of a range-top burner. Within this framework, gas composition, flow rate, and stoichiometry were varied. A detailed chemical mechanism with 71 species and 468 reactions was used to simulate the chemical kinetics. We studied general flame features, location and quantity of the pollutants carbon monoxide, nitric oxide, and formaldehyde. The fuels in these simulations were natural gas mixtures based closely on mixtures used during laboratory measurements (Singer et al. 2009) of this same study (Baseline gas, Gas 3A, and Gas 3C).

4.2. General Flame Properties

In Section 3.2 a detailed study at a single value of inflow velocity = 1 m/s and $\phi = 2.5$ is presented for the baseline gas. Supporting simulations supply gas-flow streamline information, as well as the location of the premixed and non-premixed burning. Both premixed and non-premixed regions are seen within the flame. The premixed flame front sits ≈ 0.5 cm from the inlet port, and most premixed combustion appears to be completed close (≈ 0.25 cm) and downstream of this location. Most secondary air comes from below the flame, flows laterally around, and also diffuses into the flame from bottom and sides. A small amount of secondary air is entrained into the flame from above the port. A streamline algorithm was used to visualize the general flow pattern (Figure 6), although it should be remembered that (1) advective flow only accounts for a portion of transport, with molecular diffusion also playing an important part, and (2) a higher resolution grid might result in a different streamline pattern, as more flow features are resolved.

The region of highest temperature was above the port, in the region that also had the highest CO concentration. The CO spatial contour field showed two tongue-like protuberances extending vertically (Figure 11). Comparison with the streamlines indicated that the left tongue came from flow near the center of the port and below, while the right tongue came from flow near the top of the port and possibly even entrained air.

The high-temperature region above the port is also responsible for most of the thermal NO production. Since thermal NO rises very quickly with temperature, higher NO production here is expected.

Formaldehyde is almost completely consumed within the flame, and concentrations leaving the simulation grid are on the order of 1 ppb.

4.3. Variation of Flow Velocity and Stoichiometry

We conducted a coarse sensitivity analysis by conducting simulations at velocity and ϕ values around the central point of velocity = 1 m/s and $\phi = 2.5$ (Section 3.3). Since two additional simulation points were available, they have been included in the analysis and presentation. One of these had an inflow velocity, and consequently a heat-release rate that is about double that of the other simulations.

As expected, horizontal flame extent is larger for higher inflow velocities. The trend with increasing inflow velocity (keeping ϕ constant) is for longer flame length and longer distance from the port to the point where burning commences, as well as longer flame extent in the horizontal direction. The trend with increasing ϕ (keeping velocity constant) is for a larger flame, since there is more fuel to burn. The flame front is farther from the port caused by the dependence of laminar flame speed (S_L) on ϕ, and the flame height is larger. Peak temperatures vary by about 50 K within this set of simulations, but do not show simple trends.

Likewise, air-free CO measurements taken at the top of the grid do not show a simple trend. The spatial distribution of CO indicates that at lower velocities most CO downstream of the flame is from the main jet issuing from the port; whereas, as velocity is increased a larger fraction of CO leaving the simulation appears to come from the high CO region above the port, as is apparent from the relative sizes of the left and right tongues in the CO contour spatial fields. The right tongue extends with velocity, while the left tongue stays the same or shrinks (Figure 17). Further study in this area may be instructive. Such a study would include an experimental component in which the port inclination could be varied from horizontal to vertical, while measuring change in CO emission. The logic being that for a vertical Bunsen flame the area of high CO and NO would disappear, as the flame would be symmetric. A modeling component in the study would similarly vary the port inclination. Additionally it should have a higher-resolution mesh, and perhaps also a more computationally demanding molecular diffusion scheme that uses binary diffusion or effective binary diffusion. The study should also vary both physical and thermal boundary conditions around the port, as Bunsen flames are known to be sensitive to these.

Trends with air-free NO measurements taken at the top of the grid indicate increased NO with increasing ϕ. The dependence on inflow velocity is weak.

As mentioned earlier, formaldehyde concentrations are very low, 0–1 ppb, at the top of the grid. However the simulation with high heat-release rate has a much higher formaldehyde concentration, about 14 ppb.

4.4. Effect of Gas Composition

The effect of changing gas composition, as occurs with a switch from conventional (baseline) natural gas to LNG, was analyzed in Section 3.4. Inflow velocity and ϕ were fixed at 1 m/s and 2.5, respectively, and a simulation was conducted with the baseline gas. For Gases 3A and 3C the same volumetric ratio of fuel to primary air was used, in effect as if the gas composition in the supply line had been changed. Other than the change in inflowing gas composition, there was no difference between simulations. Gases 3A and 3C have higher Wobbe number than baseline gas. From spatial plots of temperature, CO, and NO, little difference was seen between the three cases. When CO and NO were integrated and summed it was seen that the two simulated LNG mixtures (3A and 3C) had slightly higher production rates for these pollutants. A comparison of intermediate species along the oxidation paths of methane, ethane, and propane showed qualitatively why CO production was so similar between the three gas

mixtures: regardless of the fuel mixture, the quantities of intermediate species tended to converge with distance down the oxidation chain.

4.5. Quenching at the Flame Tip

The flame height is 2 to 3 cm above the port, depending on the inflow conditions. It is possible that introducing a thermally conducting, top boundary (simulating the lower surface of a cooking utensil) could induce quenching, especially in the early stage of warming. This could result in higher pollutant concentrations, especially of CO, which would be produced but not oxidized to CO_2 at the same rates that occur for an unperturbed flame. Modeling this physical configuration would require multiple changes to the modeling domain and many simulations in which the parameters varied would be boundary temperature, boundary height, and top right inflow boundary mixture (fresh/burnt air). This effort was far beyond the scope and available funding for this task.

5.0 References

Ashman, P. J., and B. S. Haynes. 1996. "Formaldehyde formation in small gas burners." *Combust Sci and Tech* 116-117: 359–373.

Bennett, B. A., and M. D. Smooke. 2005. Computational and Experimental Study of Oxygen-Enhanced Laminar Methane/Air Diffusion Flames. Proc. 4th Joint Meeting of the U.S. Sections of the Combustion Institute.

Bhatia, P. et al. 2005. CFD Based Global and Detailed Chemistry Predictions for Inverse Laminar Ethane Jet Diffusion Flames under Oxygen Enhancement and Gravity Variation. Proc. 4th Joint Meeting of the U.S. Sections of the Combustion Institute.

Bowman, C. T. 1991. *Chemistry of Gaseous Pollutant Formation and Destruction, Fossil Fuel Combustion.* Chapter 4. Eds. W. Bartok and A. F. Sarofim. John Wiley Press. ISBN 0-471-84779-8.

Brown, P. N., G. D. Byrne, A. C. Hindmarsh. 1988. "VODE, A Variable-C Coefficient ODE Solver." *SIAM J. Sci. Stat. Comput.* 1989, 10, 1038– 1051. Also, LLNL Report UCRL-98412, June.

Brun, R. 2010. Physics Analysis Workstation. http://paw.web.cern.ch/paw/.

Childs, H. et al. 2005. VisIt: A Contract Based System for Large Data Visualization. Proceedings for IEEE 2005. Minneapolis, Minnesota. https://wci.llnl.gov/codes/visit/.

Cloutman, L. D. 1990. The COYOTE CFD Code. Tech. Rep. UCRL-ID-103611. Lawrence Livermore National Laboratory.

Curran, H. J., P. Gaffuri, W. J. Pitz, and C. K. Westbrook. 1998. A Comprehensive Modeling Study of n-Heptane Oxidation. *Combustion and Flame* 114:149–177.

Dryer, F. L. 1991. *The Phenomenology of Modeling Combustion Chemistry, Fossil Fuel Combustion.* Chapter 3. Eds. W. Bartok and A. F. Sarofim. John Wiley Press. ISBN 0-471-84779-8.

Dworkin, S. B. et al. 2007. "Computational and experimental study of a forced, time-dependent, methane-air coflow diffusion flame." *Proc. Comb Inst* 31: 971–978.

Frenklach, M. et al. 1995. *GRI-Mech---An Optimized Detailed Chemical Reaction Mechanism for Methane Combustion.* Tech. Rep. GRI-95/0058. Gas Research Institute. http://www.me.berkeley.edu/gri mech/.

Gerstein, M. 1991. Diffusion Flames, Fossil Fuel Combustion. Chapter 7. Eds. W. Bartok and A. F. Sarofim. John Wiley Press. ISBN 0-471-84779-8.

Johnson, F., and D. M. Rue. 2003. *Gas Interchangeability Tests Evaluating the Range of Interchangeability of Vaporized LNG and Natural Gas.* Final Report GRI-03/0170, Gas Technology Inst. April.

Jomaas, G. et al. 2005. "Experimental determination of counterflow ignition temperatures and laminar flame speeds of C_2-C_3 hydrocarbons at atmospheric and elevated pressures." *Proc. Comb Inst* 30: 193–200.

Kazakov, A., and M. Frenklach. 2010. DRM-19 chemical mechanism. http://www.me.berkeley.edu/drm/.

Kee, R. J., F. M. Rupley, E. Meeks, J. A. Miller. 1996. *Chemkin-III: A Fortran Chemical Kinetics Package for the Analysis of Gasphase Chemical and Plasma Kinetics.* Tech. Rep. SAND96-8216, UC-405, Sandia National Laboratory.

Ortega, F. 2010. General Mesh Viewer. http://www-xdiv.lanl.gov/XCM/gmv/GMVHome.html.

Petersen, E. L. et al. 2007." Methane/propane oxidation at high pressures: Experimental and detailed chemical kinetic modeling." *Proc. Comb Inst* 31: 447–454.

Pillier, L. et al. 2005. "Influence of C_2 and C_3 compounds of natural gas on NO formation: An experimental study based on LIF/CRDS coupling." *Proc. Comb Inst* 30: 1183–1191.

Qin, Z. et al. 2000. "Combustion Chemistry of Propane: A Case Study of Detailed Reaction Mechanism Optimization." *Proc. Comb Inst* 28: 1663–1669. http://ignis.usc.edu/Mechanisms/C3-opt/C3-opt.html .

Seshadri, K., and X. S. Bai. 2007. "Rate-ratio asymptotic analysis of the structure and extinction of partially premixed flames." *Proc. Comb Inst* 31: 1181–1188.

Singer, B. C., M. G. Apte, D. R. Black, T. Hotchi, D. Lucas, M. M. Lunden, A. G. Mirer, M. Spears, and D. P. Sullivan. 2009. *Natural Gas Variability in California: Environmental Impacts and Device Performance: Experimental Evaluation of Pollutant Emissions from Residential Appliances.* California Energy Commission, PIER Energy-Related Environmental Research, Interim Report. CEC-500-2009-099. LBNL-2897E.

Torres, D. J, and M. F. Trujillo. 2006. "KIVA-4: An unstructured ALE code for compressible gas flow with sprays." *Journal of Computational Physics* 219: 943–975. http://www.lanl.gov/orgs/t/t3/codes/kiva.shtml. http://www.erc.wisc.edu/modeling/kiva.php. http://homepages.cae.wisc.edu/~hessel/manualsAndEpilogues/index_manual.html.

Walsh, T. W. et al. 2005. "A comparison of computational and experimental lift-off heights of coflow laminar diffusion flames." *Proc. Comb Inst* 30: 357–365.

Wang, H. et al. 2007. USC Mech Version II. High-Temperature Combustion Reaction Model of H2/CO/C1-C4 Compounds. http://ignis.usc.edu/USC_Mech_II.htm.

Warnatz, J.,U. Maas, and R. W. Dibble. 1995. *Combustion.* Springer-Verlag Press. ISBN 3-540-60730-7.

Williams, F. A. 2010. San Diego Mechanism. http://maeweb.ucsd.edu/~combustion/cermech.

Appendix A

Calculation of Heat Release from a Residential Burner

Appendix A: *Calculation of Heat Release from a Residential Burner*

As verification that we chose reasonable values for inflow velocities and ϕ, we compared the flame heights and dimensions to similar observed values in a residential burner with comparable heat release. The comparison is to a Magic Chef range with a stamped rating of 9,200 Btu/hr for natural gas. This has 28 big ports (diameter ≈ 2 mm), 28 medium ports (diameter ≈ 1.5 mm), and 28 small ports (diameter ≈ 1 mm). Assuming a Poiseuille flow profile through a port of radius **a**:

$$v(r) = A(a^2 - r^2)$$

(where A is a constant) and integrating flux over the port, results in total heat release proportional to a^4. If the total heat release is 9,200 Btu/hr for all 84 ports, the large 2 mm ports are 238 Btu/hr, the medium 1.5 mm ports are 75 Btu/hr, and the small 1 mm ports are 15 Btu/hr. The modeling grid has a port width of 2 mm, similar to the larger ports.

On the device with the gas turned up full, the flames from the larger ports are observed to come out horizontally about 1.5 cm and vertically between 2 and 3 cm. (The flames from the small ports are about half this size.) On the other hand, the larger ports are situated on an upper and a lower row. The flames from the lower row extend farther horizontally than those on the upper row as their flow field is influenced by the upper flames, so even this simple observation has complications.

In a modeling simulation with inflow velocity = 1.8 m/s, the heat release is 217 Btu/hr, which is close to the large 2 mm diameter port on the Magic Chef. It is difficult to say where the top of the flame is, since in the simulation there is no yellow sooting at the tip, but the flame heights appear comparable.

The conclusion from this exercise is that the (v = 1.8 m/s, ϕ = 3) case is similar to running a burner at full capacity, and the five-point design centered about (v = 1 m/s, ϕ = 2.5) corresponds to running at medium capacity, where most cooking occurs.